Improved Delayed Detached Eddy Simulations of Flow past an Autonomous Underwater Helicopter

Zhikun Wang[a], Guang Yin[1b], Muk Chen Ong[b], Ying Chen[a]

[a]Ocean College, Zhejiang University, Zhoushan 316000, China

[b]Department of Mechanical and Structural Engineering and Materials Science, University of Stavanger, N-4036 Stavanger, Norway

Abstract

To achieve good control of an Autonomous Underwater Helicopter (AUH), it is of great significance to study its hydrodynamic quantities. In the present study, hydrodynamic analysis of a disk-shaped AUH is carried out by using three-dimensional(3D) Improved Delayed Detached Eddy Simulations (IDDES) for the complex flow around an AUH model with main installed structures. The Reynolds numbers based on the incoming flow velocity and diameter of the AUH are in the range of $(4\sim8)\times10^5$. The predicted drag and lift coefficients of the AUH at 3 different incoming flow velocities (0.35m/s, 0.5m/s, 0.75m/s) with 5 different pitch angles of ($-15°$, -7.5°, 0°, 7.5°, 15°) are analyzed. When the pitch angle increases from 0° to $\pm15°$, the value of $\langle C_D\rangle$ increases from 0.50 to 0.67. The value of $\langle C_L\rangle$ decreases from 0.73 to -0.89 with the increasing pitch angle from $-15°$ to 15°. The drag and lift coefficients of the AUH at 3 different incoming flow velocities with 5 different pitch angles are analyzed. The vortical flow structures of the 3 typical pitch angle cases subjected to an incoming flow velocity of 0.5m/s are presented and discussed. A drag force element decomposition analysis is employed to further reveal the relationship between the wake flow and the hydrodynamic forces. It is found that the inverse Ultra Short Base Line (iUSBL) sensor and Global Positioning System (GPS) antenna have significant contributions to the drag force. Furthermore, Dynamic Mode Decomposition (DMD) is applied to study the large-scale wake flow structures behind the AUH. The dominant modes are selected by using a sparsity-promoted algorithm. The modal analysis results reveal the spatial distributions of the large-scale 3D flow structures. It is indicated that vortical structures at different frequencies can be generated due to the installations on the AUH and different pitch angles.

[1] Corresponding author: guang.yin@uis.no

Keywords: Autonomous Underwater Helicopter (AUH), CFD, IDDES, Dynamic Mode Decomposition

1. Introduction

The Autonomous Underwater Vehicle (AUV) is a widely used device for underwater survey tasks, including underwater environment monitoring, deep-sea seabed survey, and underwater pipeline inspection, among other scientific or engineering applications (Bondaryk, 2004; Evans and Nahon, 2004; Hagen et al., 1999; Jagadeesh et al., 2009; Neves et al., 2020; Sherman et al., 2001; Stommel, 1989; Tanakitkorn et al., 2016; Xiang et al., 2016). AUVs typically operate in complex underwater environments and their performance is influenced by hydrodynamic loads. Consequently, investigating the hydrodynamic characteristics of AUVs is crucial for improving their design and achieving good controls. Tow-tank experiments are traditionally conducted to investigate these properties but require high experimental costs. With the development of numerical simulations, Computational Fluid Dynamics (CFD) techniques provide an efficient tool for studying the hydrodynamic properties of AUVs. Jagadeesh et al. (2009) demonstrated the applicability of numerical simulations based on the Reynolds-Averaged-Navier-Stokes (RANS) method to investigate the hydrodynamic characteristics of AUVs compared to towing tank experiments. Bettle et al. (2009) studied the six degrees of freedom (6DoF) of an AUV using RANS simulations with the k-ω SST turbulence model to study the influence of the initial heel angle on the emergence roll angle and rotation rate. Although the typical torpedo-shaped AUVs provide excellent high-speed and wide-range cruise performance, achieving high maneuverability and near-seabed operating capabilities will further necessitate exploration beyond the use of traditional torpedo-shaped AUVs. A new type of disk-shaped AUV called the Autonomous Underwater Helicopter (AUH) was proposed by Zhejiang University (Chen et al., 2017, 2019). Chen et al. (2017) conducted a CFD investigation of the AUH's motion stability using RANS combined with the RNG k-ε turbulence model and obtained the drag coefficients under different pitch angles and operating velocities. Recently, Wang et al. (2019) developed a prototype of the AUH (Figure 1), which can move horizontally and vertically driven by four horizontal and two vertical thrusters installed inside tunnels. To achieve good controllability of the AUH, it is necessary to obtain the hydrodynamic forces acting on the vehicle. Several studies have investigated the flow around the AUH to determine drag, lift, and moment coefficients using both experimental measurements and numerical simulations since

its invention. Wang et al. (2019) carried out a theoretical analysis of the AUH's maneuverability and vertical motion stability, which was validated by experimental measurements. Chen et al. (2020) used numerical simulations to investigate the water entry process of an AUH, employing the Volume of Fluid (VOF) method to capture the water surface, and predicted the water entry impact forces of the AUH under different water entry velocities and angles. Lin et al. (2021) conducted numerical simulations using the same turbulence model to investigate the drag forces in the horizontal and vertical directions, considering the influence of the tunnels where the thrusters are installed on the drag forces. Guo et al. (2022) conducted experiments and CFD simulations to investigate the influence of the seabed on the hydrodynamic characteristics of an AUH and revealed that an additional lift force is generated due to the sea bottom and is sensitive to the bulges at the top and bottom of the AUH. Lin et al. (2022a) improved the hydrodynamic performance of an AUH using a fore-aft asymmetric geometry with a sharp tail, which was validated by experimental measurements and numerical simulations.

Previous numerical simulations of the hydrodynamic characteristics of an Autonomous Underwater Vehicle (AUH) typically relied on the Reynolds-Averaged Navier-Stokes (RANS) method, which allows for fast prediction of hydrodynamic quantities. However, these simulations only capture time-averaged flow characteristics and do not predict unsteady hydrodynamic behaviors. In the real sea environment, the Reynolds number of the surrounding flow defined as $Re = UD/\nu$ (where U is the characteristic velocity of the AUH in a typical range of 0.35-0.75 m/s, and D is the characteristic length scale of the AUH in a range of 0.35-2 m) is usually high, with values up to $O(10^5)$ due to the large separation flow around the AUH. This results in massive flow separation and a complex unsteady wake flow characterized by multiscale vortical flow structures which affect the unsteady hydrodynamic quantities of the AUH. These multiscale vortical structures cannot be captured by using the commonly employed RANS simulations and are difficult to measure in experiments or observations. In addition, previous studies on AUH hydrodynamics have typically used a model where all working loads were removed, neglecting the influence of various installed components such as the inverse Ultra Short Base Line (iUSBL) sensor, GPS antenna, and USBL speaker, which are crucial for the vehicle's operations (as shown in Figure 1(b)). The hydrodynamic characteristics of the AUH with these installed components have not been fully explored. Furthermore, most of the previously published studies mentioned focused on the hydrodynamic properties of the simplified AUH, and the correlation of the forces acting on the AUH with the surrounding flow behaviors is not clear.

To address these gaps in understanding the hydrodynamic characteristics of the AUH, more detailed spatial and temporal resolved simulations are required, which demand high computational costs. The present study employs detailed three-dimensional (3D) Improved Delayed Detached Eddy Simulations (IDDES) to investigate the unsteady hydrodynamic quantities and flow behaviors around an AUH. IDDES can achieve a balance between the computational cost and the numerical accuracy by combining the RANS model within the boundary layer and the Large Eddy Simulations model in the outer region to capture the multiscale unsteady vortices, especially in the wake region. The relationship between the wake flow and the forces acting on the AUH is also explored by using a drag force element analysis. Furthermore, to better understand the simulation results, the flow is analyzed using Dynamic Mode Decomposition (DMD) (Schmid 2010) to study the spatial and temporal characteristics of the dominant flow structures.

The organization of the present paper is outlined as follows. The mathematical formulation and numerical methods are given in Section 2. The convergence studies and validation studies are performed in Section 3 to assess the accuracy and reliability of the employed numerical model. The results are reported and discussed including the hydrodynamics quantities, power spectra analysis of the fluctuations, instantaneous flow structures and DMD analysis are given in Section 4. Finally, a conclusion is made for the present study.

2. Mathematical formulation and numerical method

2.1 Mathematical formulation

Hybrid turbulence models which combine the strengths of both Reynolds-Averaged Navier-Stokes simulations (RANS) and Large Eddy Simulations have become increasingly popular in CFD simulations. Among these, the Improved Delayed Detached Eddy Simulation (IDDES) method shows great potential in accurately predicting turbulent flow while maintaining computational efficiency. The IDDES method combined with the $k-\omega$ SST model is employed in the present study. The IDDES method is used to capture the unsteady turbulent eddies, and the $k-\omega$ SST model is employed to model the near-wall turbulence boundary layer. The governing equation for the incompressible flow is the filtered Navier-Stokes equations given in the framework as:

$$\frac{\partial u_i}{\partial x_i} = 0 \tag{1}$$

$$\frac{\partial u_i}{\partial t}+\frac{\partial u_i u_j}{\partial x_j}=-\frac{1}{\rho}\frac{\partial p}{\partial x_i}+\nu\frac{\partial^2 u_i}{\partial x_j \partial x_j}-\frac{\partial\langle u_i' u_j'\rangle}{\partial x_j} \tag{2}$$

where $i,j=1,2,3$ (for x,y,z) is the streamwise, spanwise directions and cross streamwise, respectively. u_1 u_2 u_3 (for u,v,w) correspond to the resolved part of the velocity components. ρ is the density of the water. The unresolved stress, denoted by $-\langle u_i' u_j'\rangle$, can be modeled by using the relationship with the strain of the resolved velocity components as

$$-\langle u_i' u_j'\rangle=\nu_t\left(\frac{\partial u_i}{\partial x_j}+\frac{\partial u_j}{\partial x_i}\right) \tag{3}$$

In the region away from the walls, the sub-grid eddy viscosity ν_t is used. In the near-wall region, the $k-\omega$ SST turbulence model-based RANS equations are solved to obtain the eddy viscosity of ν_t. For the $k-\omega$ SST model, two additional transport equations are solved to calculate the turbulence specific dissipation rate ω and the turbulence kinetic energy k, which can be found in Menter et al. (2003) and are not described here in detail. Based on the values of ω and k, the turbulence viscosity ν_t can be calculated as:

$$\nu_t=a_1\frac{k}{\max(a_1\omega,F_2 S)} \tag{4}$$

where $a_1=0.31$ and the invariant measure of strain rate S and a second blending function F_2 can be also found in Menter et al. (2003). In the SST-based DES formulation, the dissipation term of the k-equation is modified by the turbulent length scale, as proposed by Travin et al. (2002), Strelets (2001) and Krappel et al. (2015)

$$D_k=\beta^* k\omega=\frac{k^{3/2}}{l_t} \tag{5}$$

with length scales

$$l_{\mathrm{RANS}}=\frac{\sqrt{k}}{\beta^*\omega}\qquad l_{\mathrm{LES}}=C_{\mathrm{DES}}\Delta \tag{6}$$

for the RANS and LES region, where Δ is the length scale associated with the local grid spacing in the three directions expressed as

$$\Delta=\max\left(\Delta_x,\Delta_y,\Delta_z\right) \tag{7}$$

The value of C_{DES} is obtained by using different constants for the $k-\varepsilon$ and $k-\omega$ regions in the SST framework as

$$C_{\mathrm{DES}}=(1-F_1)C_{\mathrm{DES},k-\varepsilon}+F_1 C_{\mathrm{DES},k-\omega} \tag{8}$$

where F_1 denotes the SST blending function, which can also be found in Menter et al. (2003). The model constants are $C_{\mathrm{DES},k-\varepsilon}=0.78$ and $C_{\mathrm{DES},k-\omega}=0.61$. To address the issue of "grid-induced separation" (GIS), DDES is proposed by delaying the transition from RANS in the

attached boundary layer region to LES in the separation region. In the SST framework, the DDES length scale is represented as

$$l_{\mathrm{DDES}} = l_{\mathrm{RANS}} - f_d \max(0, l_{\mathrm{RANS}} - l_{\mathrm{LES}}) \tag{9}$$

where f_d is the empiric blending function. Furthermore, the present employed IDDES method combines DDES and Wall-Modeled LES (WMLES), and the length scale is implemented according to Shur et al. (2008):

$$l_{\mathrm{IDDES}} = \tilde{f}_d(1 + f_e) l_{\mathrm{RANS}} + \left(1 - \tilde{f}_d\right) l_{\mathrm{LES}} \tag{10}$$

$\tilde{f}_d$ is the blending function for the IDDES method, which is an improved version of f_d accounting for the effect of wall modeling and f_e is the elevating function, which is introduced to improve the blending between RANS and LES in the employed IDDES method. Detailed information on the numerical method can be found in Gritskevich et al. (2012).

2.2 Numerical methods

The open-source Computational Fluid Dynamic (CFD) code OpenFOAM is utilized to carry out the simulations in the present study. The PIMPLE scheme is used, which combines the Pressure Implicit with Splitting of Operators (PISO) scheme and Semi-Implicit Method for Pressure Linked Equations (SIMPLE) scheme. The spatial schemes for gradient, Laplacian, divergence, and interpolation are least Square, Gauss linear limited corrected, Gauss linear upwind and linear, respectively.

3. Computational overview

3.1 AUH model

The AUH designed by Zhejiang University is used as the test model, as shown in Figure 1 (a). The diameter of AUH is $D = 1.5\mathrm{m}$. A sea trial of the prototype has been completed in the South China Sea. The Reynolds number defined by the characteristic velocity U_∞ and the diameter D of the AUH is set to be $Re = 4 \times 10^5$. Due to the high computational cost of the 3D simulations for the wake flow behind the AUH with various installations, a simplification of the AUH model is necessary to capture the large-scale wake flow features and the general hydrodynamic characteristics. The simplified model is shown in Figure 1 (b), where most of the small features on the surfaces and inside the AUH are removed, and only the main installations are retained, such as a GPS antenna, an Ultra Short Base Line (USBL) speaker and an inverse USBL (iUSBL) receiver.

(a)

(b)

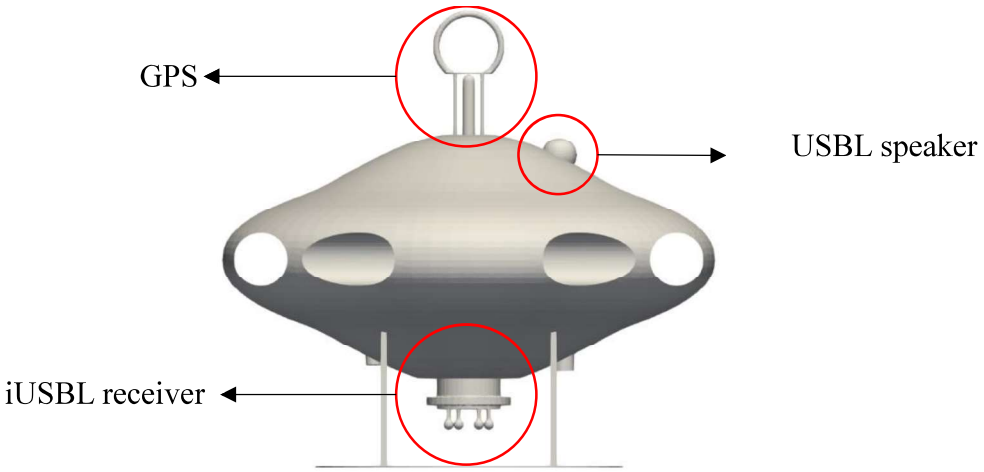

Figure 1. (a) A prototype of the AUH; (b) The model of the AUH.

3.2 Computational domain

The computational domain, as shown in Figure 2, is centered on the oblate-shaped AUH with the origin of the coordinates located at the center of the AUH. The width and height of the computational domain are $15D$, and the length is $22.5D$. The distance between the inlet boundary and the center of the AUH is set to be $7.5D$. The distance between the outlet boundary and the center of the AUH is set to be $15D$. Based on previous studies, for example, in Chen et al. (2020), the size of the computational domain is 16m×5m×8m for an AUH with the dimensions of 2m×1m×1m. In Lin et al. (2021), the size of the computational domain is 10

m×10 m×15 m for an AUH with a diameter of 1.5m. In Guo et al. (2022), the size of the computational domain was set to be $9.3D \times 6D \times 3.3D$ with the characteristic length of D for an AUH. According to these studies, the present adopted computational sizes can be regarded as sufficiently large. The other parameters of the IDDES simulations can be based on the study reported by Ohmichi et al. (2019). The boundary conditions for the simulation are set as follows:

(1) No-slip condition ($\boldsymbol{u = v = w = 0}$) is applied on the surface of the AUH. The pressure is set to be zero normal gradient. The standard wall function is applied for the near-wall region to resolve the values of $\boldsymbol{k}$ and $\boldsymbol{\omega}$. A wall function based on the Spalding's law of the wall (Spalding 1961) is used to resolve $\boldsymbol{\nu_t}$.

(2) At the outlet boundary, the velocities and $\boldsymbol{\nu_t}$ are set to be zero normal gradient, and the pressure is set to be a fixed value of zero.

(3) At the inlet boundary, a fixed inlet value of $\boldsymbol{U_\infty}$ is used for the flow velocity and the pressure is set to zero gradient.

(4) The symmetry boundary conditions are used for all the other boundary planes, including the top, bottom, front and back.

The simulations are performed using a parallel computing technique, dividing the computational domain into 64 subdomains for each case.

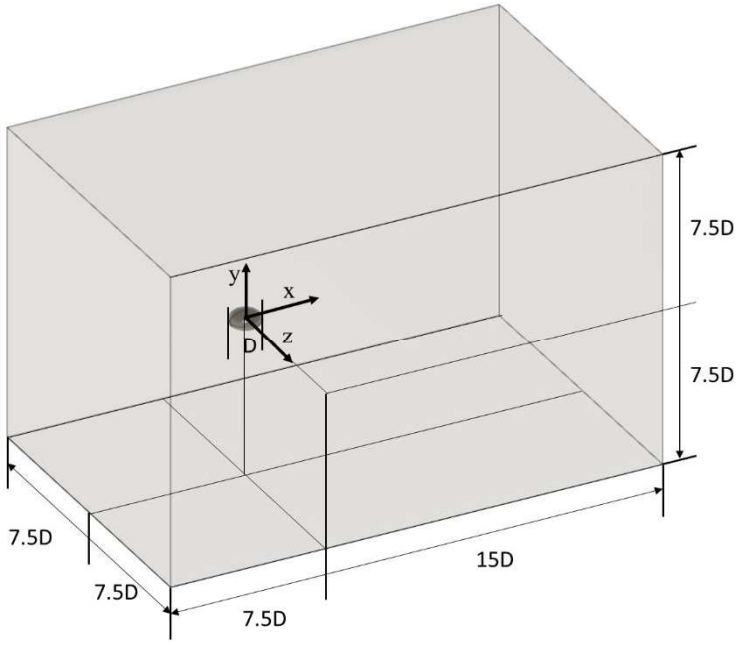

Figure 2. The computational domain for the simulations.

3.3 Convergence studies

To determine the necessary grid resolution for the simulations, mesh convergence studies are conducted. Three different meshes with a progressively refined grid resolution are generated using cfmesh, an open-source mesh tool within the framework of openFOAM. The mesh is generated with a base grid size of 0.4. To achieve good computational accuracy, the grid around the AUH is refined by using several refinement boxes.

The time-averaged drag coefficient $\langle C_D \rangle$ is used to evaluate the mesh convergence, which is defined as:

$$\langle C_D \rangle = \frac{\langle F_x \rangle}{0.5\rho U_\infty^2 A_x} \tag{11}$$

where $\langle F_x \rangle$ is the time-averaged value of the total force obtained by integrating the pressure and shear stress acting on the surface of AUH in the x direction. U_∞ is the inlet velocity. ρ is the fluid density. A_x is the projection area of AUH in the x direction. A preliminary test is carried out to determine the window size of obtaining the time-averaged values. Table 1 shows an example of the preliminary test with a grid size of 4.7×10^6 elements and an inlet velocity of 0.35 m/s. The relative differences between $\langle C_D \rangle$ for each time window size are within 1%, indicating that a window size of 100 s is reasonable.

The values of $\langle C_D \rangle$ for the three meshes are shown in Figure 4. The results of $\langle C_D \rangle$ for the meshes M1 with 2.4×10^6 elements and M2 with 4.7×10^6 elements are 0.473 and 0.496, respectively. The difference in the mesh size between M1 and M2 is 96% with a relative difference of 4.86% in the $\langle C_D \rangle$ value. The results of M2 with 4.7×10^6 elements and M3 with 7.1×10^6 elements are 0.496 and 0.503, respectively. The difference in the mesh size between M1 and M2 is 51% with a relative difference of less than 1.5%. Therefore, the mesh M2 with 4.7×10^6 elements can be considered as sufficient to provide a good grid resolution and is used for all the simulations in the present study. Figure 3 shows an example of the mesh on several 2D planes of the mesh M2 in the three directions and several local regions around the AUH. The location, size and cell size of each refinement region (with the labels of Zones 1, 2, and 3 denoted in Figure 3) are shown in Table 1. The resulting time-averaged value for the maximum, minimum and averaged values of y^+ are 18.9, 0.09 and 4.34, respectively. Since a single universal formula of the turbulent velocity profile is used over the whole range of the near-wall region covering the viscous sublayer, the buffer layer and the log layer by the Spalding's law, the present employed wall function based on the Spalding's law can be regarded as appropriate.

Table 1. Results for the preliminary test with 4.7×10^6 elements and 0.35 m/s inlet flow velocity.

Window size (s)	Start time (s)	$\langle C_D \rangle$
75	50	0.492
75	75	0.490
75	100	0.495
75	125	0.498
100	100	0.496

Table 2. The locations, sizes and grid sizes of the refinement region

Zone No.	Box center (x, y, z)	Box length (L_x, L_y, L_z)	Cell size
1	(-8.5, 0, 0.655)	(10 3.5 3)	0.2
2	(-1.5, 0, 0.655)	(7 3.5 3)	0.08
3	(-0.5, 0, 0.75)	(4 2.5 2)	0.04

(a)

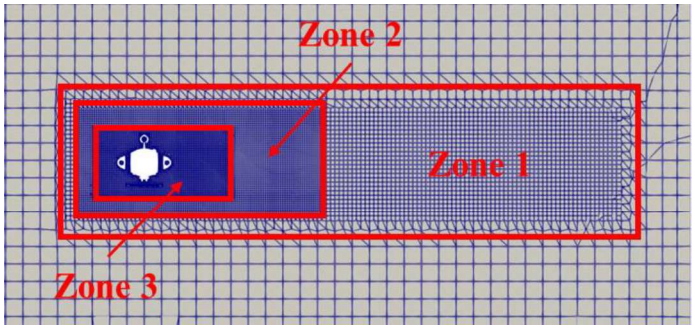

(b)

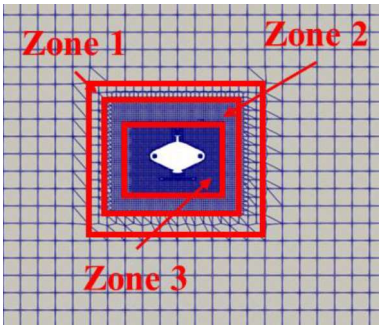

(c)

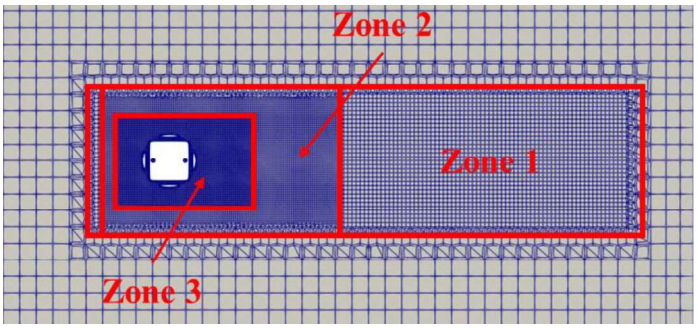

(d)

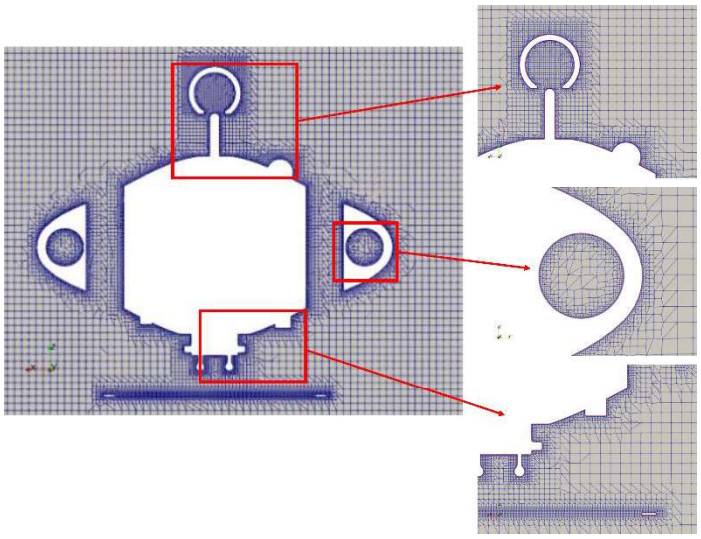

Figure 3. An example of the meshes in (a) the XZ plane; (b) the YZ plane and (c) the XY plane. (d) The grid around the AUH in the XZ plane.

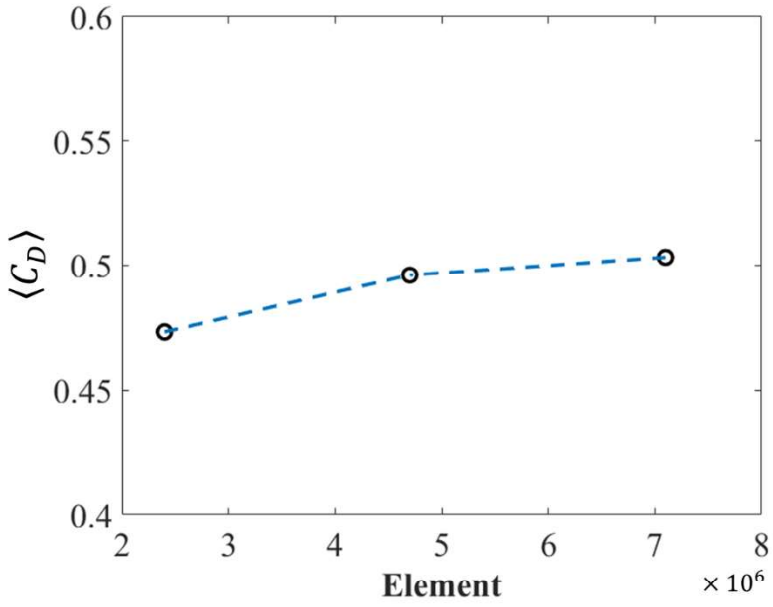

Figure 4. The values of $\langle C_D \rangle$ obtained by using different numbers of elements.

3.4 Validation studies

To validate the numerical model adopted in the present study for simulating the hydrodynamic coefficients of the AUH, the numerical model is applied for oblate spheres which have similar shapes to the investigated AUH and the results are compared against the published experimental data. A similar grid resolution to the mesh M2 is used to carry out the simulations for the oblate spheres. Two cases with two different aspect ratios λ (defined as the ratio between the revolution axis and the major axis $\lambda = b/a$, as shown in Figure 5) are conducted. The results of the comparison of $\langle C_D \rangle$ are shown in Table 3. The result of the simulation for $\lambda = 1/2$, which is similar to that of the investigated AUH, shows satisfactory agreement with the experimental data, with a minimum relative difference of less than 1% at the Reynolds number of 1.75×10^5 and the maximum relative difference of 7% at the Reynolds number of 4.0×10^5. Considering that there existed experiment uncertainties and there is no reliable experimental data available for the hydrodynamic coefficients of the present investigated AUH, this validation study can provide confidence in the ability of the numerical model to accurately predict the hydrodynamic quantities of the AUH.

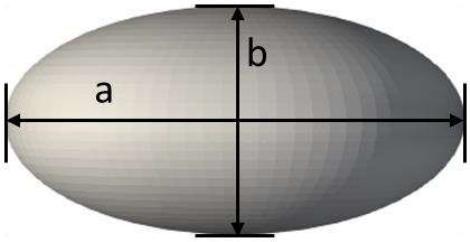

Figure 5. The shape of an oblate sphere for the validation study.

Table 3. Comparison of the experimental data and simulation results of the oblate sphere. $\langle C_D \rangle_{\mathrm{exp}}$ is experimental data reported by Uchida et al. (1981), $\langle C_D \rangle_{\mathrm{sim}}$ is the result of the present simulation.

	$\lambda = 1/2$ $Re = 1.75 \times 10^5$	$\lambda = 2/3$ $Re = 1.75 \times 10^5$	$\lambda = 1/2$ $Re = 4.0 \times 10^5$
$\langle C_d \rangle_{\mathrm{exp}}$	0.71	0.65	0.65
$\langle C_d \rangle_{\mathrm{sim}}$	0.71	0.60	0.58

Moreover, to validate the present turbulence modelling by using LES in the wake region, the energy spectra of the resolved cross-stream velocity fluctuations obtain at three representative points in the wake region behind the AUH are shown in Figure 6. It can be seen that the inertial subrange of the energy spectra follows well with the Kolmogorov spectra with a -5/3 slope, which can confirm that the LES simulations in the wake region can capture the inertial subrange of the resolved energy spectra for the present IDDES.

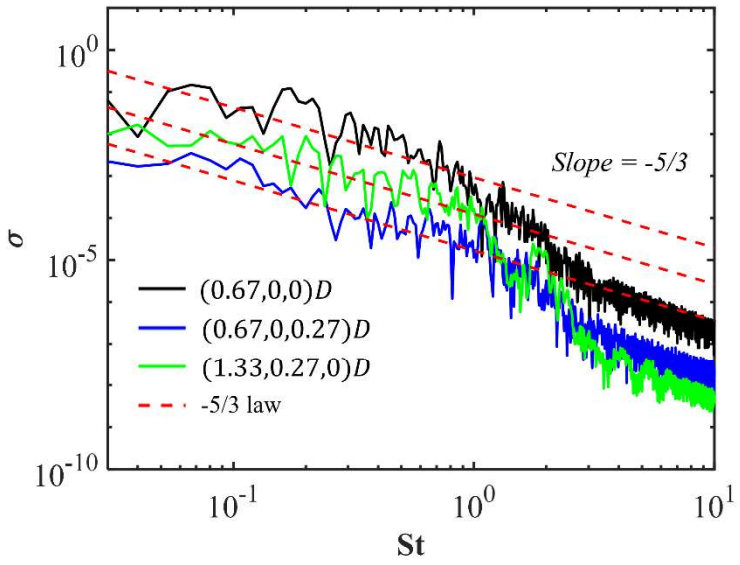

Figure 6. The power spectral at three representative points compared with the $-5/3$ law.

4. Results and discussion

4.1 Hydrodynamic forces

The hydrodynamic forces acting on the AUH, which are the most important results of the CFD simulations, are discussed in this section for different inlet flow velocities (0.35 m/s, 0.5 m/s and 0.75 m/s) and different pitch angles ($-15°$, $-7.5°$, $0°$, $7.5°$, $15°$) of the AUH. An example of different pitch angle cases is shown in Figure 7. The time-averaged values and the maximum deviation from the time-averaged values are shown in Figure 8. It is observed that both the time-averaged value and the amplitude of C_D increase with the pitch angle. Similarly, C_L also shows an increase in the time-averaged value, which is even larger than that of C_D. However, the increase in the amplitude of C_L is not significant. Due to the non-symmetrical shape of the AUH resulting from the difference in the shapes of the iUSBL sensor and GPS antenna, the C_D values are different when the AUH sails in positive and negative pitch angles. The time-averaged values of C_D in positive pitch angles are slightly larger than those in negative angles. However, as the incoming flow velocity increases, the influence of the asymmetrical shape of the AUH is reduced. A possible reason for this may be resulted from a generally increasing momentum-dominant effect of the incoming flow and a reduced viscous effect caused by the installations with the increasing flow velocity. For the highest investigated incoming flow velocity of 0.75 m/s, C_D becomes almost the same in positive and negative pitch angles, as shown in Figure 8 (a). In contrast, the asymmetrical shape has no significant effect on C_L at low incoming flow velocities while at high incoming flow velocities, C_L become non-

zero at 0° pitch angle due to the installations, which are different from those of symmetry oblate spheres.

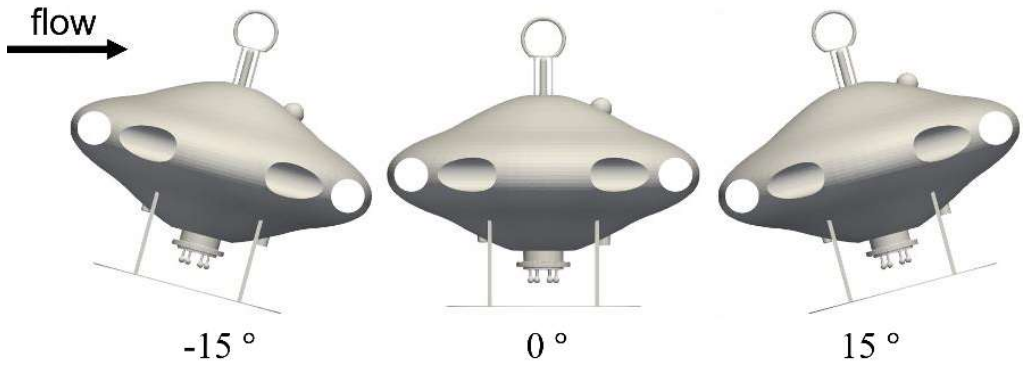

Figure 7. The AUH at the pitch angle of $-15°$, $0°$ and $15°$.

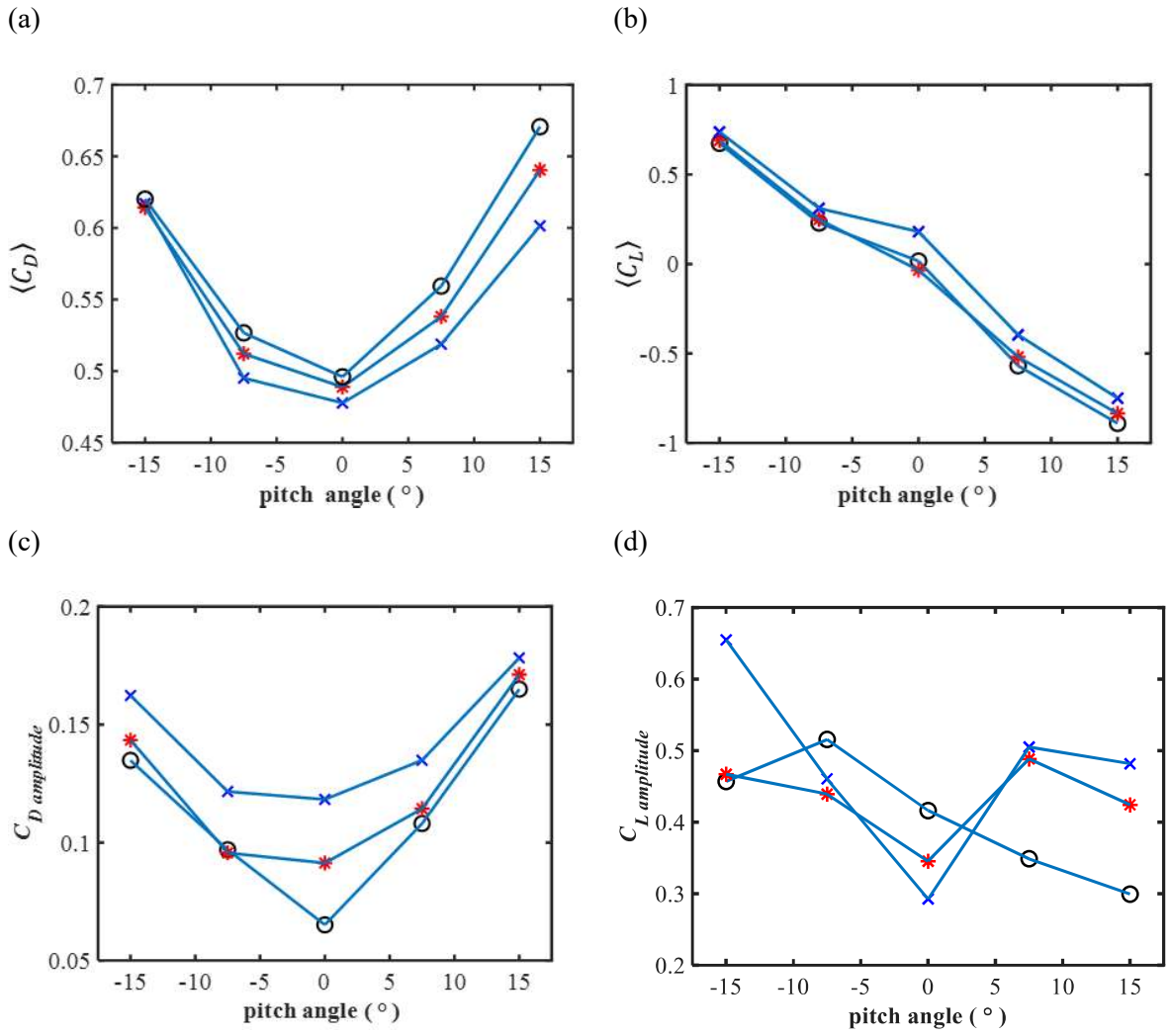

Figure 8. The time-averaged values of (a) C_D; (b) C_L and the maximum amplitudes of (c) C_D; (d) C_L under the incoming flow velocity of 0.35 m/s (black circles), 0.5 m/s (red stars) and 0.75 m/s (blue crossings).

The time history of C_D and C_L for the inlet flow velocity of 0.5 m/s at three different pitch angles of $0°$, $15°$ and $-15°$ are shown in Figure 9. For the pitch angle of $0°$, the time history of C_D exhibits some quasi-periodic characteristics and shows high and low drag regimes. The periodicity is not significant for the C_L time history. Due to the non-symmetric shape of the AUH, the C_L time history shows more chaotic behavior than C_D and displays asymmetry with respect to 0. The chaotic behavior of C_L can be also observed from the disordered phase-space plot of C_L and C_D shown in Figure 10 (a), where the correlations between the two quantities can be hardly observed, which is different from those observed in Tian et al. (2014) and Yin and Ong (2021). With the increasing pitch angle, the quasi-periodicity of C_D seems to disappear and compared with that for the $0°$ pitch angle case, more small-scale disturbances can be seen from the C_D time histories. In addition, the time history of C_L shows non-zero values and from the $C_D - C_L$ phase-space plots in Figures 10 (b) and (c), there is an obvious positive correlation between the two force coefficients and this correlation is more significant for the $15°$ pitch angle case, where the phase trace is narrowed between the two straight lines in Figure 10 (b).

(a)

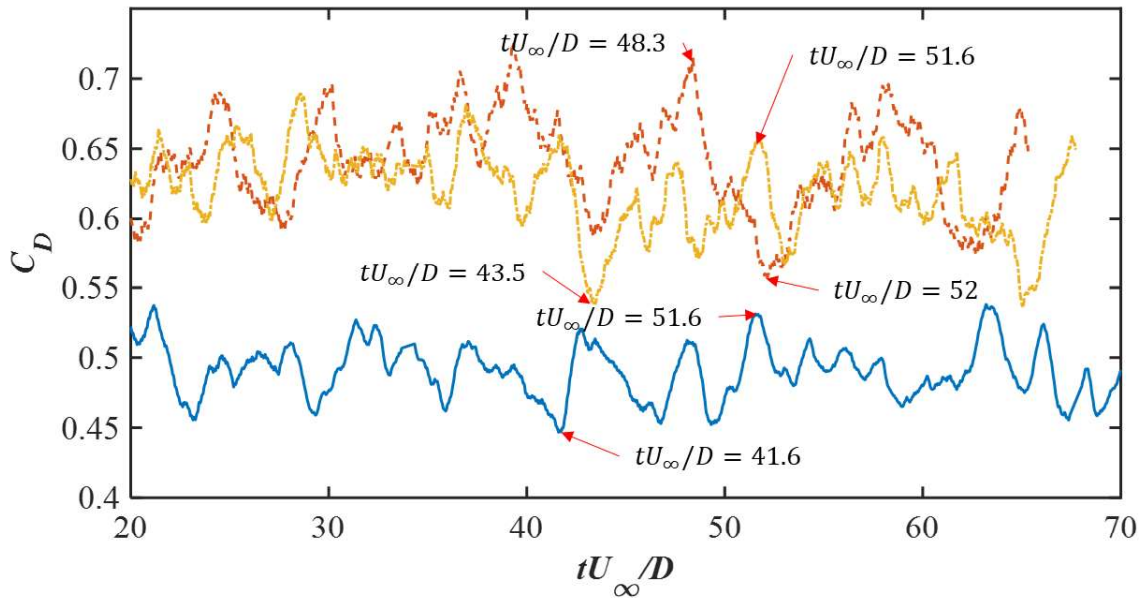

(b)

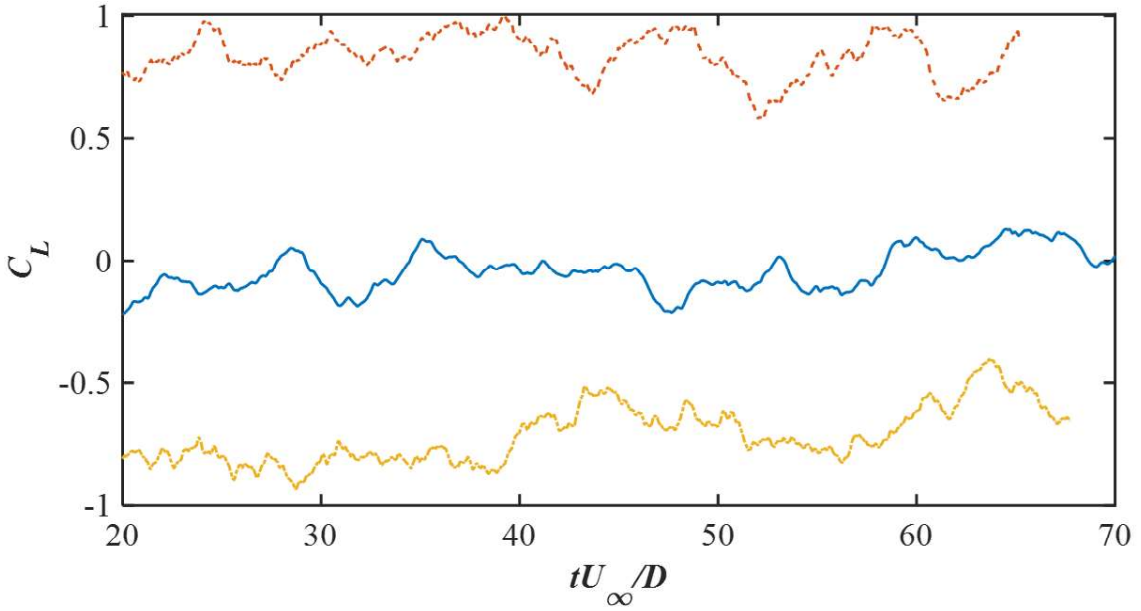

Figure 9. The time histories of (a) C_D and (b) C_L under the incoming flow velocity of 0.5 m/s at (a) 0° pitch angle (blue solid line); 15° pitch angle (red dashed line); −15° pitch angle (yellow dotted line).

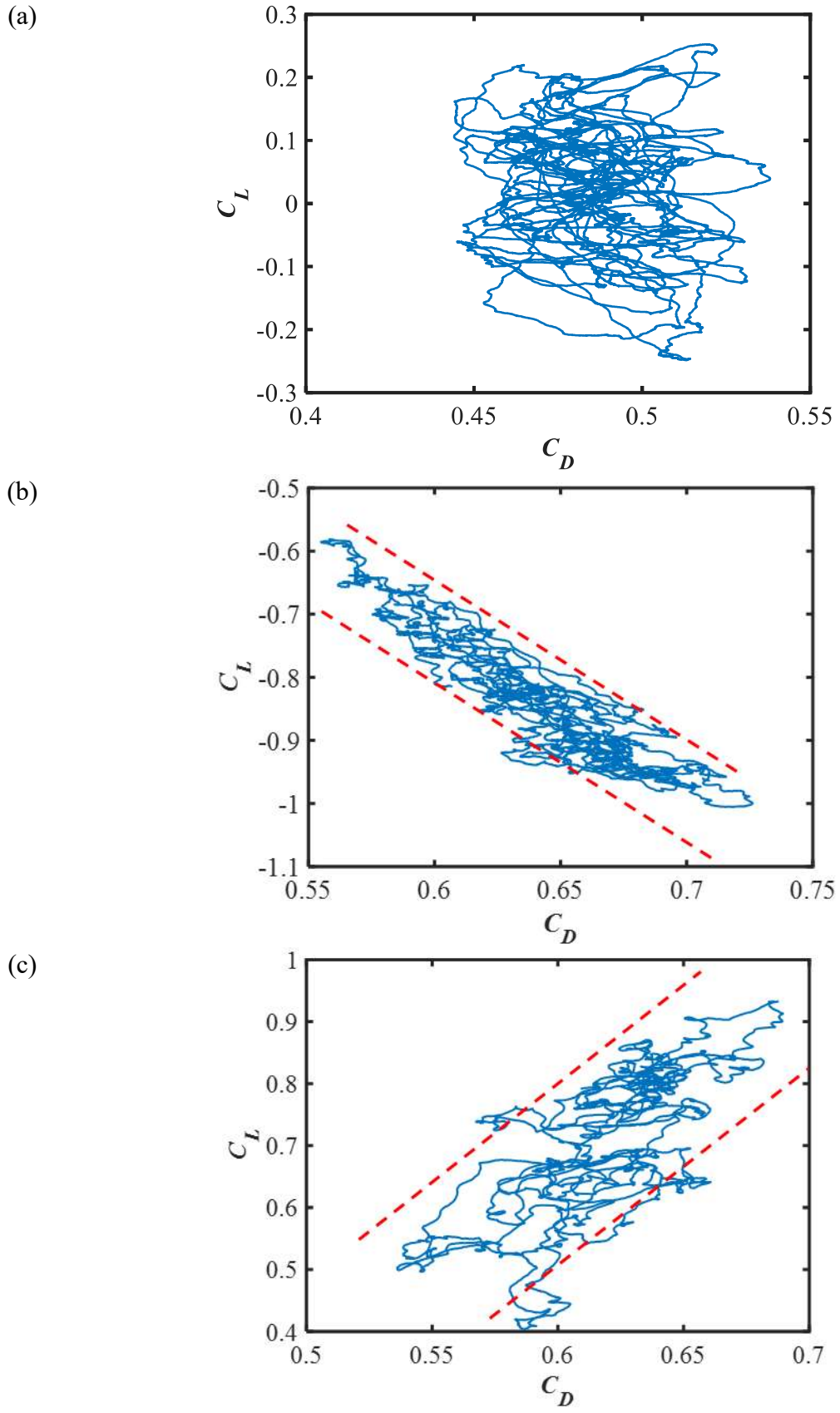

Figure 10. The phase-space plot of the C_D and C_L at (a) 0° pitch angle; (b) 15° pitch angle; (c) $-15°$ pitch angle.

4.2 Instantaneous flow structures

The vortical structures of the $U_\infty = 0.5$ m/s cases are selected for analysis and shown in Figure 11. The λ_2 isosurfaces method proposed by Jeong and Hussain (1995) is used to identify the vortical structures. Figure 11 shows the 3D view, the side view and the top view of the three pitch angles.

For the 0° pitch angle case shown in Figure 11 (a), several hairpin vortices can be observed behind the AUH. These flow instabilities appear immediately after the wake boundary layer separates from the surface, which is different from the wake flow past a spherical body as reported in Rodriguez et al. (2010, 2011). The flow instabilities lead to hairpin vortices rolled up in different directions. In the wake region, the vortices become highly three-dimensional, and their sizes become larger. For the 15° pitch angle case (Figure 11 (b), (b1), (b2)), the distribution of vortices is more compacted towards the upper part of the AUH. Except for the shear layer separated from the frame, only small-scale flow structures can be observed shed from the iUSBL and seem to be quickly dissipated. The alternately shedding from the top and bottom is hard to be observed, whereas the shedding from the right and the left side is more significant. For the −15° case (Figures 11 (c), (c1) and (c2), the vortices also become more compact compared with the 0° case, but they are gathered around the lower part of the AUH. The separation of the boundary layer seems to happen earlier at the leading edge compared with the other two cases, as shown in Figure 11 (a) and (b). The differences are obviously caused by the iUSBL sensor and GPS antenna. From the top views shown in Figure 11 (a2), (b2), and (c2), it is obvious that there are separated hairpin vortices chains from the two lateral sides of the AUH for the ±15° cases. For the 0° case, the boundary layer seems to be attached on the two lateral sides and separation occurs in the rear part. These observations highlight the sensitivity of the complex wake flow structures behind the AUH to the changes in the pitch angle.

(a)

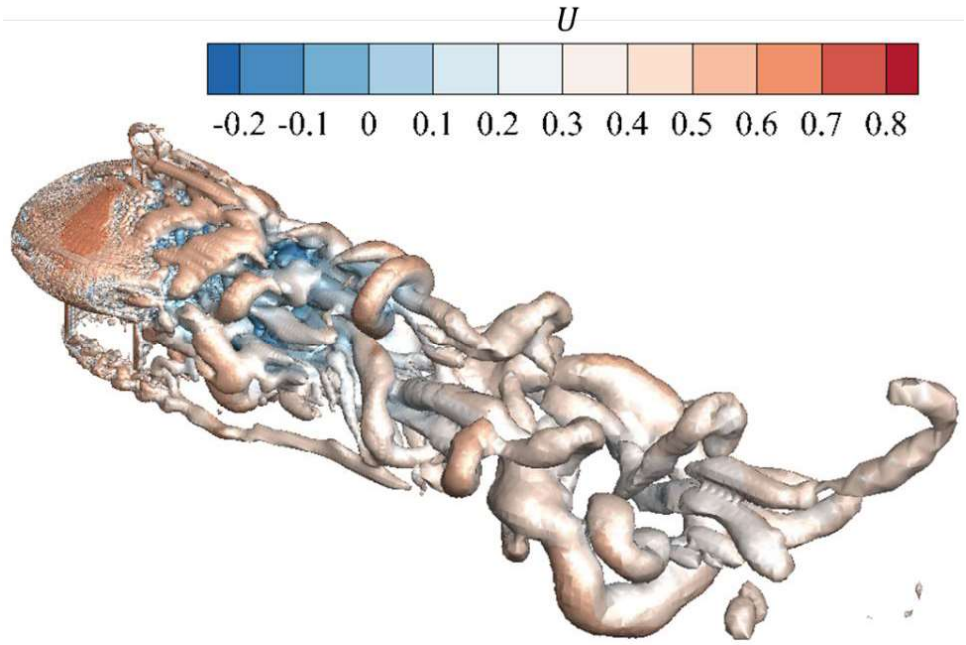

(a1)

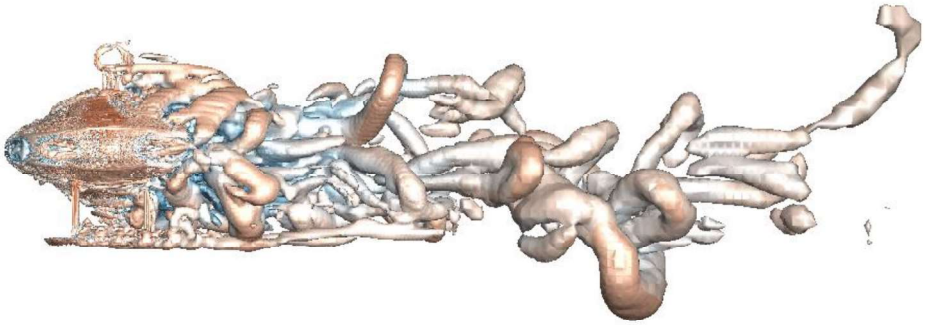

(a2)

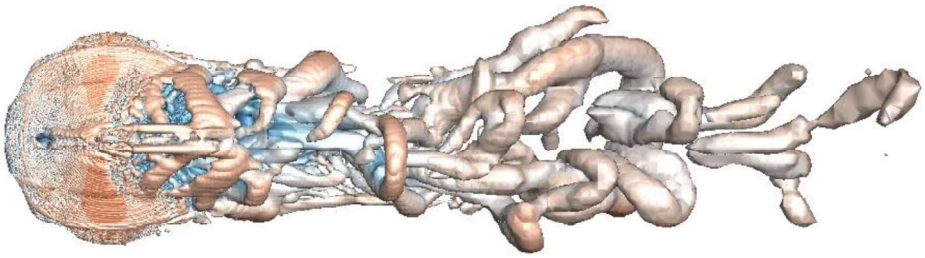

(b)

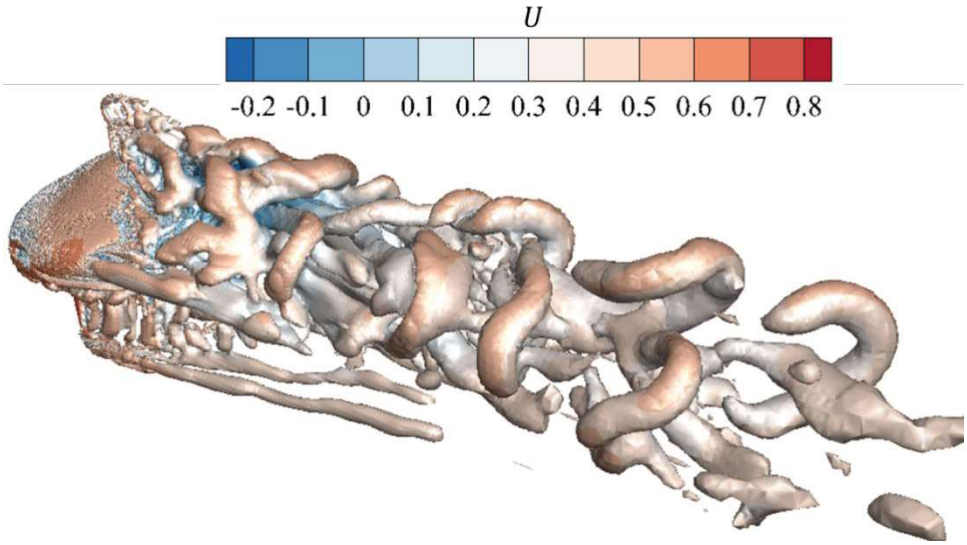

(b1)

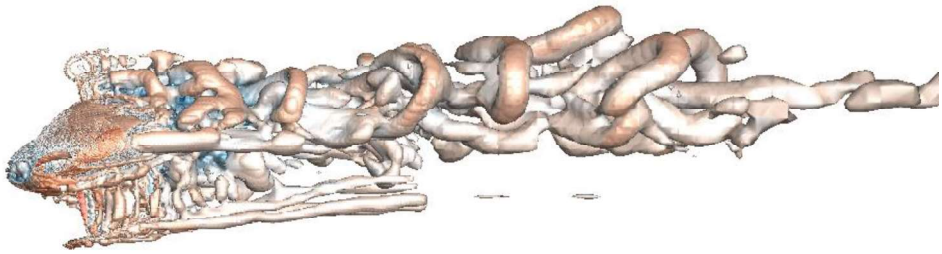

(b2)

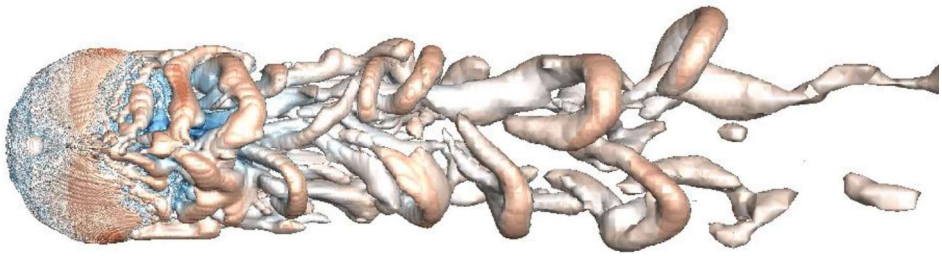

(c)

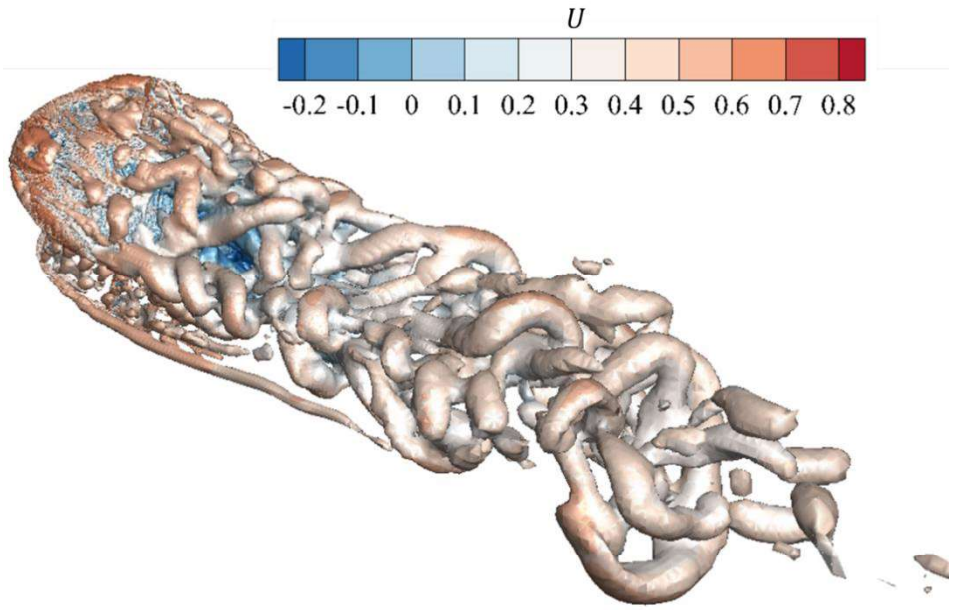

(c1)

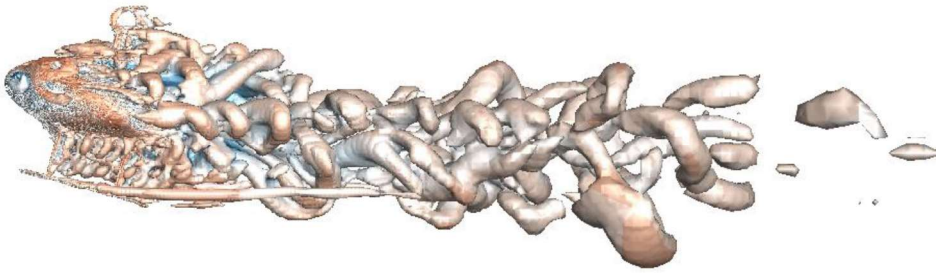

(c2)

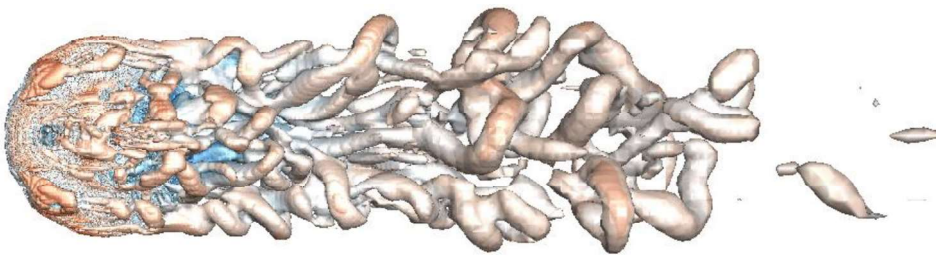

Figure 11. The instantaneous vortical structures around the AUH ($U_\infty = 0.5\mathrm{m/s}$) identified by the iso-surfaces of $\lambda_2 = -1$ colored by the streamwise velocity. (a) the three-dimensional view; (a1) the side view and (a2) the top view of the 0° pitch angle case. (b) the three-dimensional view; (b1) the side view and (b2) the top view of the 15° pitch angle case. (c) the three-dimensional view; (c1) the side view and (c2) the top view of the $-15°$ pitch angle case.

4.3 Drag force element analysis

To further quantify the contribution of the surrounding flows to the drag forces, the force element theory is used to identify dominant wake flow structures exerting hydrodynamic forces on the AUH. The force element theory is proposed by Chang (1992) and a similar analysis has been adopted by Lee et al. (2012), Zhang et al. (2020), Menon & Mittal (2021) and Ong & Yin (2022) to reveal the relationship between the flow structures and the hydrodynamic forces. An auxiliary drag potential θ_D is employed, which satisfies $\nabla^2\theta_D = 0$ within the domain and satisfies the boundary conditions of $-\mathbf{n}\cdot\nabla\theta_D = \mathbf{n}\cdot\mathbf{i}$ on the AUH surface and $\mathbf{n}\cdot\nabla\theta_D = 0$ on the outer boundaries of the flow field ($\mathbf{i}$ is the unit vector in the streamwise direction and $\mathbf{n}$ is the unit vector on the AUH surface). It should be noted that this drag potential is only related to the shape of AUH, instead of the surrounding fluid flow. By using the potential θ_D, the pressure force on AUH can be decomposed into a volume integration of the wake flow quantities and a surface integration by taking the inner product of $\nabla\theta_D$ with the momentum equation of the Navier-Stokes equations:

$$\int p\mathbf{n}\cdot\mathbf{i}\mathrm{d}S = \int \mathbf{v}\times\boldsymbol{\omega}\cdot\nabla\theta_D\mathrm{d}V - \nu\int \mathbf{n}\times\boldsymbol{\omega}\cdot\nabla\theta_D\mathrm{d}S \tag{12}$$

and the viscous drag force can be expressed as $-\nu\int \mathbf{n}\times\boldsymbol{\omega}\cdot\mathbf{i}\mathrm{d}S$. The total drag force can be expressed as:

$$F_D = \int \mathbf{v}\times\boldsymbol{\omega}\cdot\nabla\theta_D\mathrm{d}V - \nu\int \mathbf{n}\times\boldsymbol{\omega}\cdot(\nabla\theta_D+\mathbf{i})\mathrm{d}S \tag{13}$$

Compared with pressure force, the effect of viscous drag force on the AUH can be ignored at high Reynolds numbers. A detailed derivation of Eq. (12) and (13) can be found in Chang (1992), Lee et al (2012), Zhang et al. (2020), Menon & Mittal (2021) and Ong & Yin (2022).

Therefore, the contribution of the velocity and vorticity to the drag force can be quantified without relating to the solution of the Poisson equation of the pressure as shown in Hemmati et al. (2019). The values of the volume integrals $C_{DV} = \int \mathbf{v}\times\boldsymbol{\omega}\cdot\nabla\theta_D\mathrm{d}V\,/0.5U_\infty^2A$ result in the drag coefficient of the AUH. The instantaneous iso-surface of its integrands represented as $DE_V = \mathbf{v}\times\boldsymbol{\omega}\cdot\nabla\theta_D$ at two time steps corresponding to the low drag and high drag regimes (denoted in Figures 9 (a)) in the three different pitch angles (0°, 15°, −15°) cases with $U_\infty = 0.5\mathrm{m/s}$ are shown in Figure 13. The iso-surfaces of $DE_V = 0.1$ and the contours of DE_V on three selected planes defined in Figure 12 are analyzed. For the 0° case shown in Figures 13 (a1) and (a2), it can be observed that most of the drag contributions come from the separated shear layers over the back face of the AUH in the wake region. The attached boundary layer in the front face of the AUH makes negative contributions to the total drag force as shown in the

XZ plane in Figures 12 (a1) and (a2). From the XY planes, significant positive drag contributions are located in the rear corner behind the horizontal propeller tunnels. A small difference in the structures of DE_V can be observed between the low and high drag regimes. When comparing the sectional view of the YZ and XY planes between Figures 13 (a1) and (a2), the structure of DE_V under the high drag condition tends to be located closer to the AUH than the low drag regime. A similar phenomenon was also reported in Ong and Yin (2022), where at the high drag regimes, the iso-surfaces of DE_V are rolled up into the recirculation region of the body. However, the rolling-up of the shear layer is not strong compared with that behind a flat plate because the AUH is a more streamlined body than a normal flat plate, and the circulation region is much smaller and weaker than that behind a normal flat plate. From the YZ views, the circular-shaped contributions of the separated shear layer seem to be more irregular and tend to shrink towards the AUH at the high drag time step in Figure 13 (a2) compared with those at the low drag regime in Figure 13 (a1). Their strengths also seem to become stronger at the high drag regime. In addition, some of the DE_V are located around the installations and some tunnels for propellers. Especially, the iUSBL sensor-sized structures have significant effects on the drag force, while the structures in the size of GPS antenna have small contributions. The front vertical propeller tunnel has effects on the drag force while the rear one does not.

For the 15° case, the DE_V structures become more irregular and deformed compared with the 0°case especially for the low drag regime shown in Figure 13 (b1), indicating a more chaotic instantaneous drag coefficient as displayed in Figure 9 (a). The iso-surfaces shift towards the rear region of the AUH. There are also negative contributions from the boundary layer around the rear end of the AUH as seen in the XZ and YZ planes in Figure 13 (b1). At the high drag regime, the overall wake DE_V structures become much stronger compared with that at the low drag regime as observed from the larger volume occupied by the DE_V iso-surfaces in Figure 13 (b2) compared with Figure 13 (b1). The negative contributions around the rear end are reduced as shown in the XZ plane in Figure 13 (b2). Also, the influence of the frame at the lower part of the AUH becomes more significant compared with the 0° case as shown in Figures 13 (a) and (b). For the -15° case, the early separation of the boundary layer contributes to the drag force as seen in Figures 13 (c1) and (c2). Obvious positive contributions with multiple structures can be observed after the GPS as observed from the contours in the XZ plane in Figures 13 (c1) and (c2). The shrink of the DE_V structures with high amplitudes is apparently observed in the YZ plane in Figure 13 (c2) at the high drag regime. Moreover, for both two

pitch cases, the contribution of the front vertical propeller tunnel to the drag force increases significantly compared with that at the 0° pitch angle. There is almost no strong DE_V inside the back vertical tunnel except for the high drag regime shown in Figure 13 (b2) where there is even a negative contribution in the back tunnel. The effect of the iUSBL sensor becomes larger and the structure is closer to AUH as shown in Figure 13 (b). The DE_V structure appears in the horizontal propeller tunnel which does not exist in the 0° case, indicating that the horizontal propeller tunnel has a contribution to the drag force for the two pitch cases.

Therefore, it can be concluded that the installations on the AUH with different sizes have different contributions to the drag force, especially for the pitch cases. The size of the GPS antenna can be ignored, while the iUSBL sensor-sized structures should be considered when designing for drag reduction. If a large-size installed structure cannot be avoided, keeping it in front of AUH during pitch oscillation will help reduce the drag force.

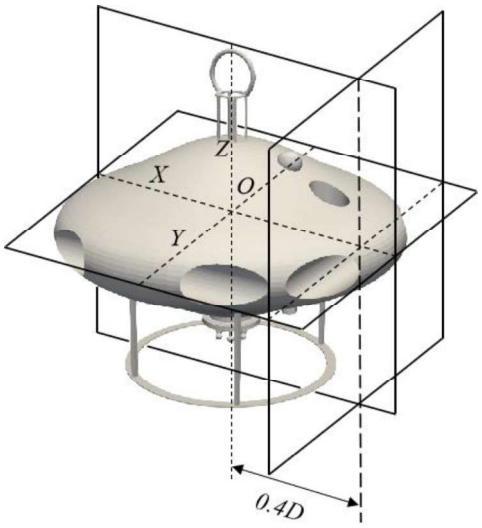

Figure 12. The locations of the planes to show the contours of DE_V for the drag force element analysis.

(a1)

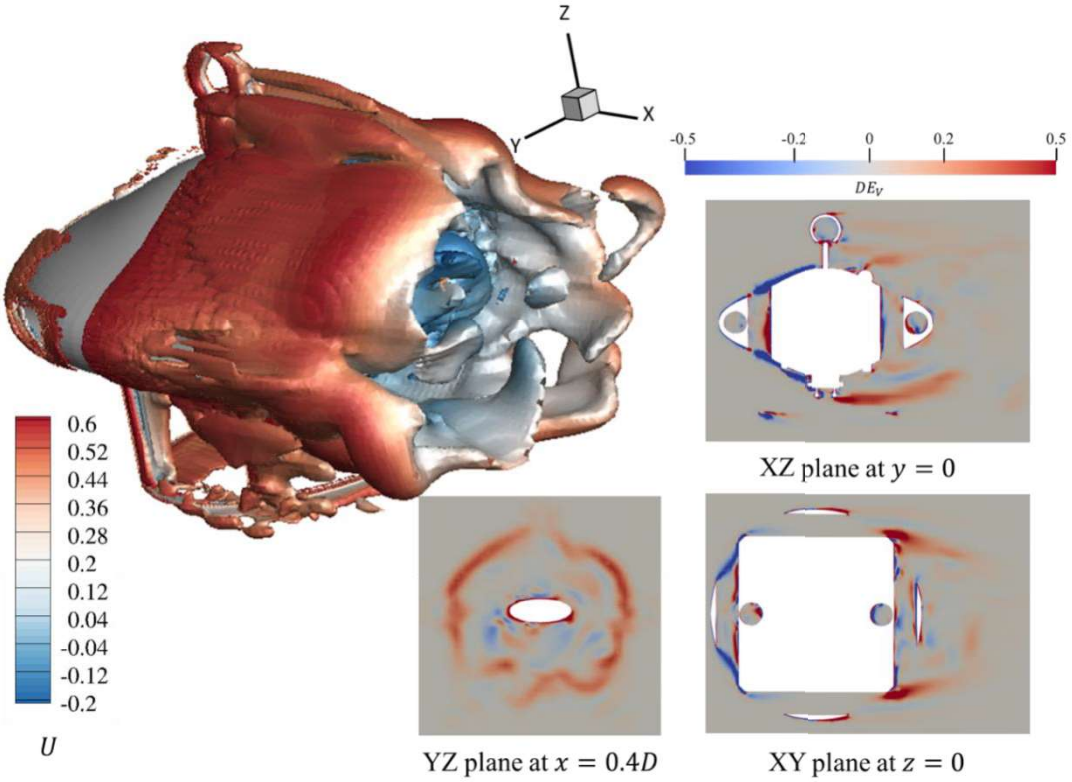
Z
X
Y
-0.5
-0.2
0
0.2
0.5
DE_V
0.6
0.52
0.44
0.36
0.28
0.2
0.12
0.04
-0.04
-0.12
-0.2
U
XZ plane at $y = 0$
YZ plane at $x = 0.4D$
XY plane at $z = 0$

(a2)

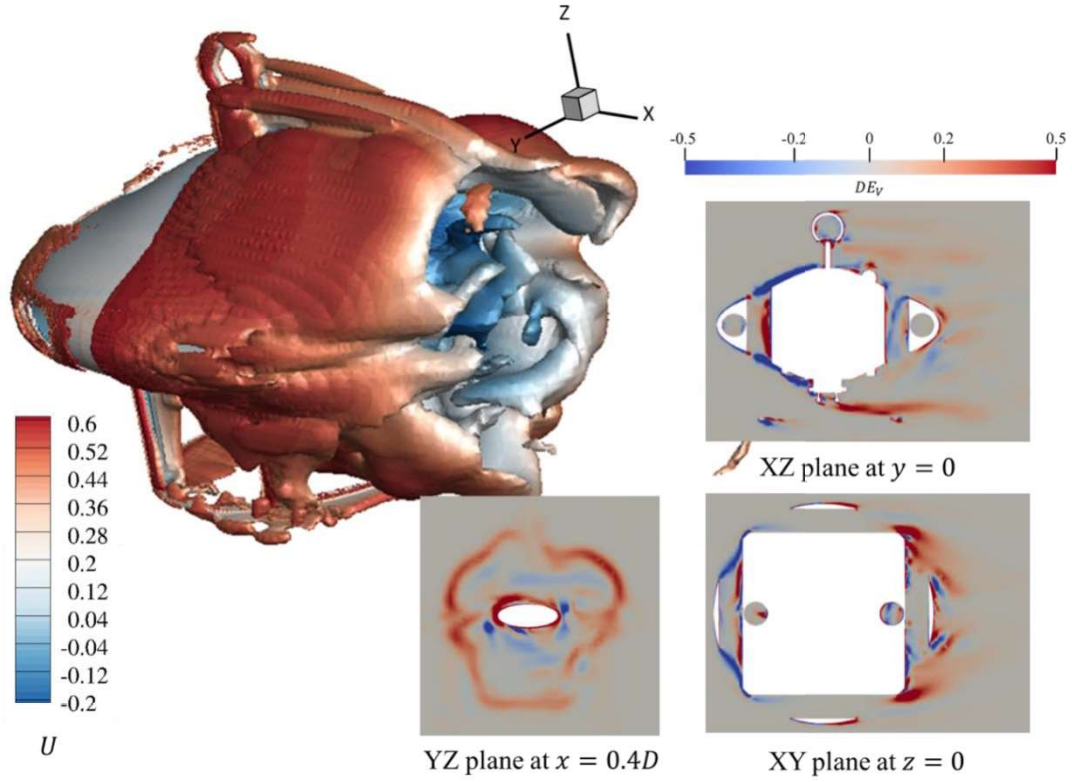
Z
X
Y
-0.5
-0.2
0
0.2
0.5
DE_V
0.6
0.52
0.44
0.36
0.28
0.2
0.12
0.04
-0.04
-0.12
-0.2
U
XZ plane at $y = 0$
YZ plane at $x = 0.4D$
XY plane at $z = 0$

(b1)

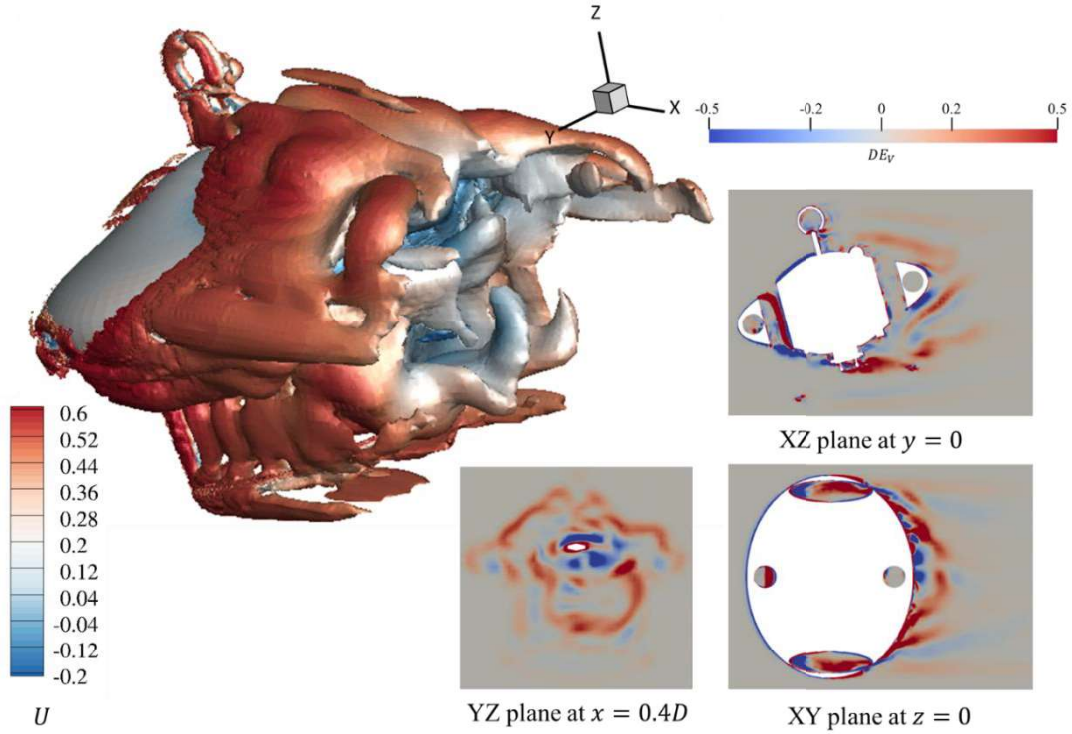
Z
X
Y
-0.5
-0.2
0
0.2
0.5
DE_V
0.6
0.52
0.44
0.36
0.28
0.2
0.12
0.04
-0.04
-0.12
-0.2
U
XZ plane at $y = 0$
YZ plane at $x = 0.4D$
XY plane at $z = 0$

(b2)

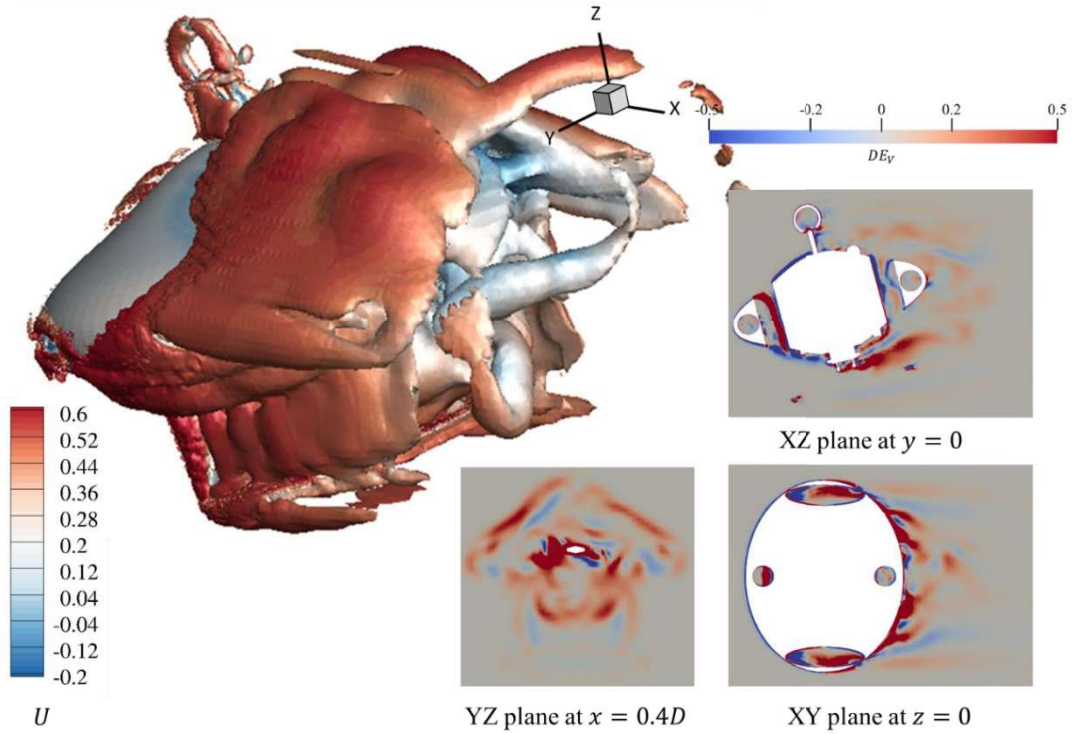
Z
X
Y
-0.5
-0.2
0
0.2
0.5
DE_V
0.6
0.52
0.44
0.36
0.28
0.2
0.12
0.04
-0.04
-0.12
-0.2
U
XZ plane at $y = 0$
YZ plane at $x = 0.4D$
XY plane at $z = 0$

(c1)

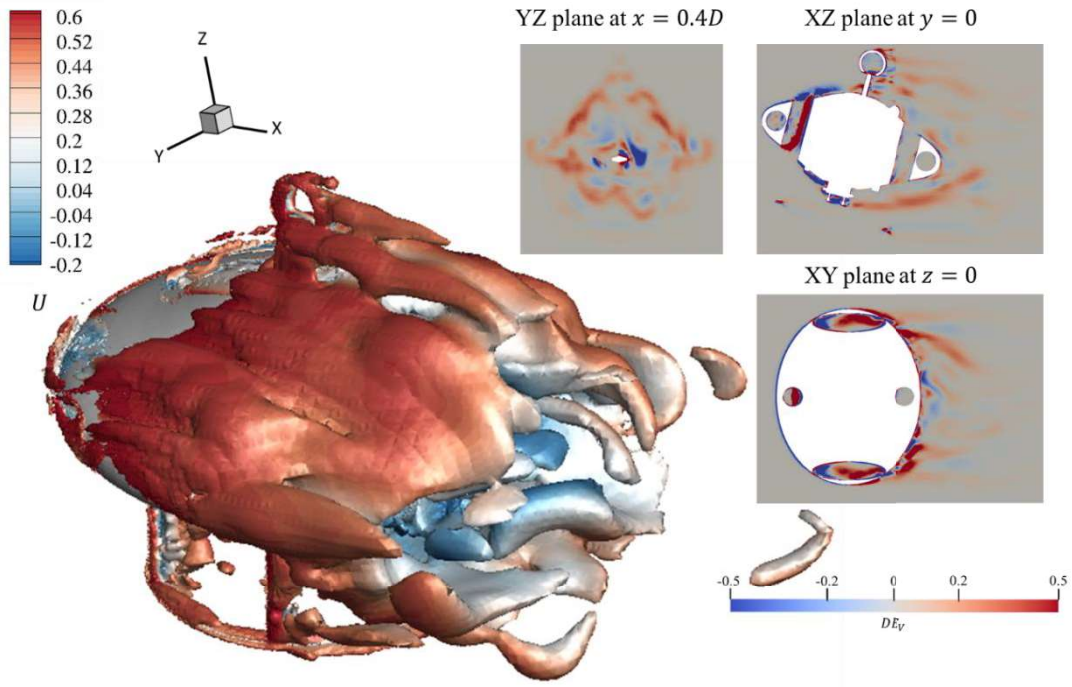

(c2)

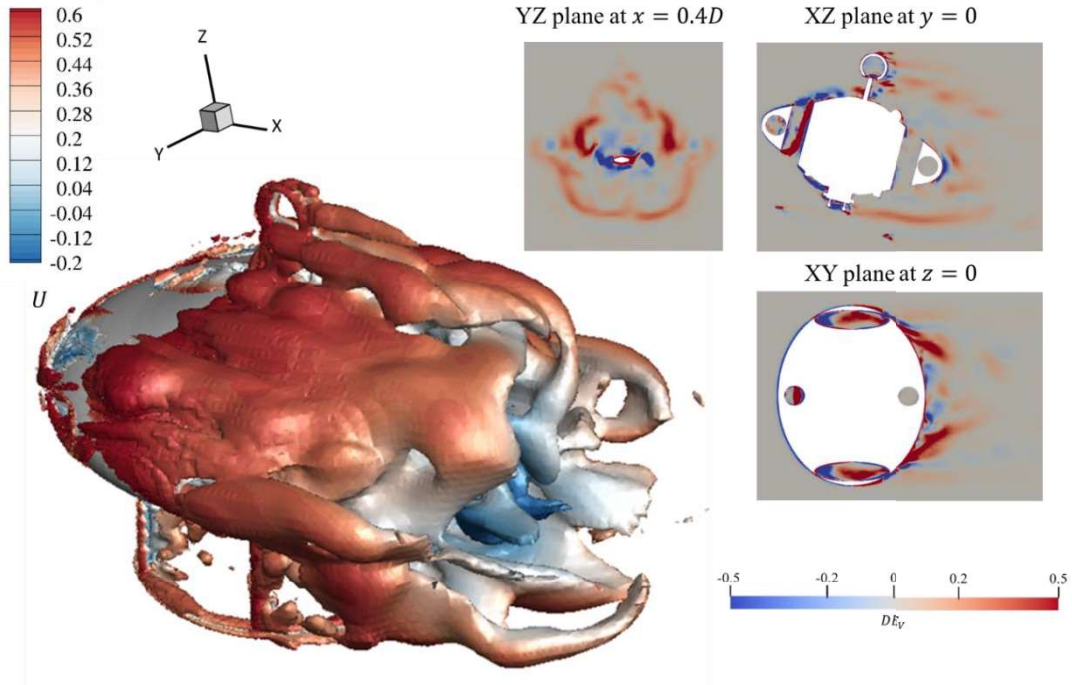

Figure 13. The three-dimensional instantaneous iso-surfaces of $DE_V = 0.1$ at (a1) the low drag time step of $tU_\infty/D = 41.6$, and (a2) the high drag time step of $tU_\infty/D = 51.6$ of the 0° pitch angle case; (b1) the low drag time step of $tU_\infty/D = 52$, and (b2) the high drag time step of $tU_\infty/D = 48.3$ of the 15° pitch angle case; (c1) the low drag time step of $tU_\infty/D = 43.5$, and (c2) the high drag time step of $tU_\infty/D = 51.6$ of the $-15°$ pitch angle case.

4.4 Dynamic mode decomposition analysis

The dynamic mode decomposition (DMD) method developed by Schmid (2010) is used to analyze the dynamic features of the flow around the AUH in this section. For a dynamic system, it is assumed that there is a linear operator $\mathbf{A}$ between two consecutive snapshots of the system as:

$$\mathbf{v_{i+1}} = \mathbf{A}\mathbf{v_i} \tag{14}$$

where $\mathbf{v_i}$ denotes the state of the system at time step $t = t_i$, which is usually the column vector of velocities and pressure stored at every node in the flow field in the present CFD analysis. Using the state vector $\mathbf{v_i}$, the input datasets can be constructed as two matrices:

$$\mathbf{V}_1^N = [\mathbf{v}_1, \mathbf{v}_2, \mathbf{v}_3, \dots \mathbf{v}_N] \in R^{N_x \times N} \tag{15}$$

$$\mathbf{V}_2^N = [\mathbf{v}_2, \mathbf{v}_3, \mathbf{v}_4, \dots \mathbf{v}_{N+1}] \in R^{N_x \times N} \tag{16}$$

Here, N_x denotes the total number of the measured signals at all observation nodes for the numerical simulations. The relationship between the two data sequence matrices can be written as:

$$\mathbf{V_2^N} = \mathbf{A}\mathbf{V_1^N} \tag{17}$$

The objective of the DMD method is to determine the eigenvalues and eigenvectors of the unknown operator $\mathbf{A}$. The eigenvalue of the operator describes the dynamical properties inherent in the data sequence. Generally, the pseudoinverse of a matrix $\mathbf{V_1^N}$ is used to compute $\mathbf{A}$. However, since N_x is the same as the nodes number of nodes in the mesh, it is always larger than the number of the snapshots N. To address memory size limitations, a low dimensional representation of the input datasets is achieved by using singular value decomposition (SVD) for the dataset $\mathbf{V_1^N}$ as:

$$\mathbf{V_1^N} = \mathbf{U}\mathbf{\Sigma}\mathbf{V}^T \tag{18}$$

where $\mathbf{\Sigma}$ is a diagonal matrix containing non-zero singular values on its diagonal. $\mathbf{U}$ and $\mathbf{V}$ contain orthogonal unit columns and the column vectors of $\mathbf{U}$ are the proper orthogonal decomposition (POD) modes of the datasets $\mathbf{V_1^N}$. Then, Eq. (18) can be expressed as:

$$\mathbf{V}_2^N = \mathbf{A}\mathbf{U}\mathbf{\Sigma}\mathbf{V}^T \tag{19}$$

$$\mathbf{A} = \mathbf{V}_2^N\mathbf{V}\mathbf{\Sigma}^{-1}\mathbf{U}^T \tag{20}$$

A reduced-order representation of $\mathbf{A}$ can be computed by projecting $\mathbf{A}$ onto $\mathbf{U}$ instead of directly calculating the eigenvalues of A. This representation is as follows:

$$\widetilde{\mathbf{A}} = \mathbf{U^T}\mathbf{A}\mathbf{U} = \mathbf{U^T}\mathbf{V_2^N}\mathbf{V}\mathbf{\Sigma}^{-1} \qquad \left(\widetilde{\mathbf{A}} \in R^{N \times N}\right) \tag{21}$$

Because of the orthogonality of the column vector of $\mathbf{U}$, the reduced-order representation $\widetilde{\mathbf{A}}$ has the same eigenvalues as $\mathbf{A}$. Then, solving the eigenvalue problem results in the following:

$$\widetilde{\mathbf{A}}\mathbf{Y} = \mathbf{Y}\boldsymbol{\Lambda} \tag{22}$$

Here, $\boldsymbol{\Lambda} = \mathrm{diag}(\mu_1, \mu_2, \ldots \mu_N)$ contains the eigenvalues of $\widetilde{\mathbf{A}}$ and $\mathbf{A}$. The columns of $\mathbf{Y}$ are the eigenmodes of $\widetilde{\mathbf{A}}$. By using matrix $\mathbf{U}$, the corresponding eigenmodes of $\mathbf{A}$ are obtained by $\boldsymbol{\Phi} = \mathbf{U}\mathbf{Y} = [\boldsymbol{\phi}_1, \boldsymbol{\phi}_2, \ldots \boldsymbol{\phi}_N]$. The eigenmodes are referred to as the DMD modes. According to Schmid (2010), the frequency St and amplification rate σ of the mode can be represented as $St = \mathrm{Im}(\log(\mu_i)/2\pi\Delta t)$ and $\sigma = \mathrm{Re}(\log(\mu_i)/2\pi\Delta t)$. The next step in the DMD analysis is to identify the physically dominant modes, which can be accomplished through the use of the sparsity-promoting (SP) DMD method proposed by Jovanović et al. (2014). This algorithm was further improved and adopted to analyze the low Re flow past a circular cylinder by Ohmichi (2017) and this method was also used to analyze the flow past an atmospheric entry capsule at high Re in Ohmichi et al. (2019).

By using the DMD modes ϕ_i and their corresponding eigenvalue μ_i, the input dataset can be approximated as:

$$\mathbf{V}_1^N \approx \boldsymbol{\Phi}\mathbf{D}_\alpha\mathbf{V}_{\mathrm{and}} = [\boldsymbol{\phi}_1, \boldsymbol{\phi}_2, \boldsymbol{\phi}_3 \ldots \boldsymbol{\phi}_\mathbf{N}] \begin{bmatrix} \alpha_1 & & \\ & \ddots & \\ & & \alpha_N \end{bmatrix} \begin{bmatrix} \mu_1^0 & \cdots & \mu_1^{N-1} \\ \vdots & \ddots & \vdots \\ \mu_N^0 & \cdots & \mu_N^{N-1} \end{bmatrix} \tag{23}$$

where α_i denotes the amplitude of each DMD mode. These values indicate the contribution of the DMD modes to the dynamic system. The most dominant modes can be selected by solving an optimization problem as:

$$\min_{\alpha} \|\mathbf{V}_1^N - \boldsymbol{\Phi}\mathbf{D}_\alpha\mathbf{V}_{\mathrm{and}}\|_2 \tag{24}$$

where $\|\cdots\|_2$ is the Frobenius norm of a matrix. According to Jovanović et al. (2014), to achieve the balance between the accuracy and the number of the dominant modes, a penalty γ is introduced. This results in the following optimization problem:

$$\min_{\alpha} \left(\|\mathbf{V}_1^N - \boldsymbol{\Phi}\mathbf{D}_\alpha\mathbf{V}_{\mathrm{and}}\|_2 + \gamma \sum_{i=1}^{N} |\alpha_i| \right) \tag{25}$$

When using a large value of γ, most of the α_i becomes 0, which means the SPDMD method selects the most contributing modes in the dynamic system and removes other modes.

In the present study, the SPDMD algorithm is performed on the (u, v, w) data obtained from the 3D computational domain. DMD analysis is carried out on cases with the inlet velocity of 0.5m/s of the designed speed of the AUH and 3 pitch angles. A similar 3D DMD analysis was also performed by Ohmichi et al. (2019) on the flow around a capsule. For the present study, the number of the snapshots is $N = 200$ taken from the time span of $33.3 \leq tU_\infty/D \leq 66.7$ with a time step of $\Delta tU_\infty/D = 0.167$.

The DMD eigenvalues of the three cases are shown in Figure 14. According to Schmid (2011) and Pan et al. (2015), when the eigenvalue of a DMD mode is located on a unit circle, the growth/decay rate of the mode is zero, and the mode can be considered as 'neutrally stable'. As shown in Figure 14 (a), (c), (e), most of the eigenvalues are located on the unit circle, indicating that most of the DMD modes of the turbulent flow around the AUH are statistically stationary. However, there are also a few eigenvalues located inside the unit circle and they have negative growth rates. As reported in Jovanović et al. (2014), these modes are strongly damped within the temporal evolution of the dynamical system. By comparing Figures 14 (c) and (e) with (a), it can be observed that the number of these damped modes in the non-zero pitch angle cases is obviously more than that in the zero-pitch angle case. This difference may be due to more small-scale flow structures induced by the installations at the top and bottom of the AUH, which are quickly dissipated. Also, the number of these modes is slightly higher for the negative pitch angle than that for the positive angle.

The power spectral of the DMD modes as well as the modes selected by the SPDMD are shown in Figures 14 (b), (d), (f). Most of the modes are removed by using the SPDMD with a high γ, indicating that these modes are quickly damped during the time evolution and have little contribution to the dynamic system. Among the remaining modes after applying the SPDMD method, the most dominant mode corresponds to the time-averaged flow with a frequency of 0 in all three different pitch angle cases. Except for the zero-frequency mode, the oscillatory modes appear as a pair of complex conjugate modes. Therefore, one mode from each pair is selected and analyzed. The characteristics of these modes differ for different pitch angles. In general, for the 0° pitch angle case, all the remaining modes are low-frequency modes within the range of $St \leq 0.2$. For the $\pm 15°$ pitch angle cases, in addition to the low-frequency modes, high-frequency modes at $St > 0.5$ also appear as dominant.

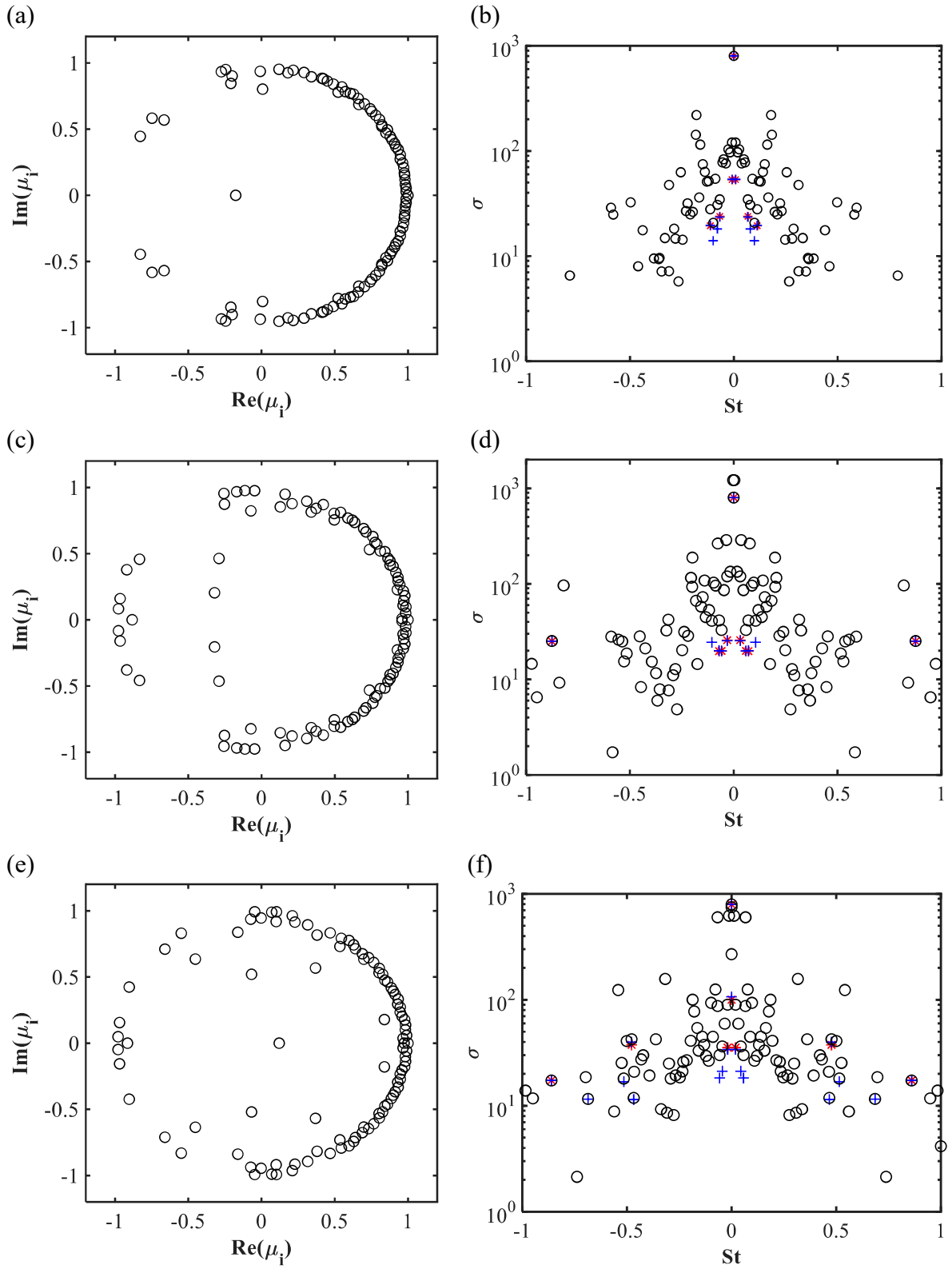

Figure 14. The DMD eigenvalues for the cases of (a) 0°, (c) 15°, (e) −15° pitch angle. (b), (d), (f) are the DMD spectral at the three pitch angles, respectively. (Black circles: all DMD modes; Blue crossings: selected by SPDMD with $\gamma = 222$ for the 0° pitch angle case and $\gamma = 205$ for the $\pm 15°$ cases; Red stars: selected by SPDMD with $\gamma = 235$ for the 0° case and $\gamma = 222$ for the 15° case and $\gamma = 239$ for the −15° case.)

The DMD spectral with the frequencies $St > 0$ of the dominant modes and a low γ is shown in Figure 16. Since the wake flow displays multiscale temporal features, all the spectral are widely distributed. A comparison between the DMD spectral and the power spectral densities (PSD) of the velocity signals for the three pitch angle cases is made and shown in these figures. The PSDs are obtained using the fast Fourier transformation with Welch's method (Welch 1967). To collect the time series of the u, v and w signals, 27 probes are set around the AUH and the locations of the probes are shown in Figure 15. The sampling frequency is $\Delta t U_\infty / D = 0.0167$ and the time span of the sampling is $T U_\infty / D = 40$.

As shown in Figure 16 (a), in the case of 0° pitch angle, most of the dominant frequencies are within a low-frequency range of 0~0.1. A small peak can be observed at $St = 0.55$. The distribution of the remaining modes is generally consistent with the PSD. For the 15° pitch angle case shown in Figure 16 (b), the dominant frequencies have a wider distribution in the range of 0~0.3 with another high-frequency peak appearing at around $St = 0.85$. However, because of the installations, the performance of the $-15°$ pitch angle case shown in Figure 16 (c) is not exactly the same as the 15° case. The range of dominant frequencies is narrower than those for the 15° case, with more modes located around $St = 0.5$ for the $-15°$ case. Furthermore, the DMD modes can correspond to different frequency peaks in the PSD of the velocity signals at different wake locations. They can be viewed as a combination of POD and the Fourier transformation, as mentioned in Taira et al. (2017). Hence, the DMD modes can capture both the spatial structures and temporal evolution of the dominant flow structure, which is a good way to analyze the flow structures with the dominant DMD modes instead of the primitive flow field.

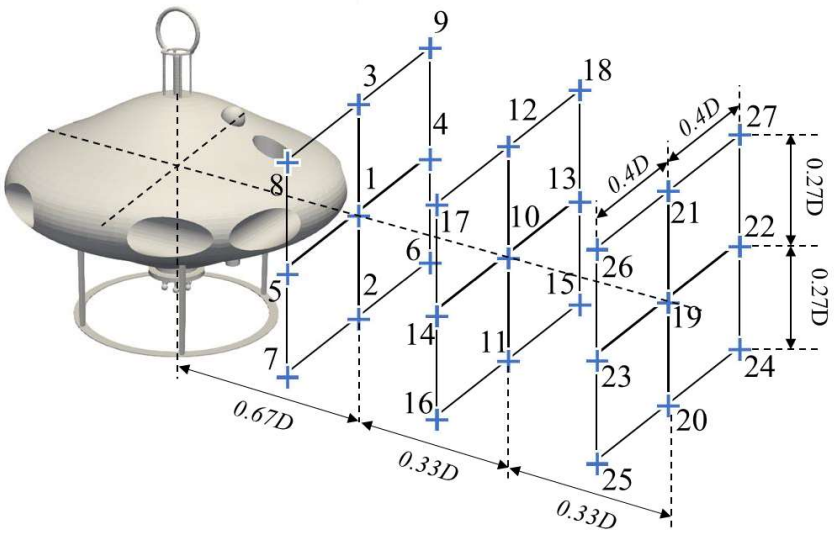

Figure 15. The locations of the probes for the PSD analysis

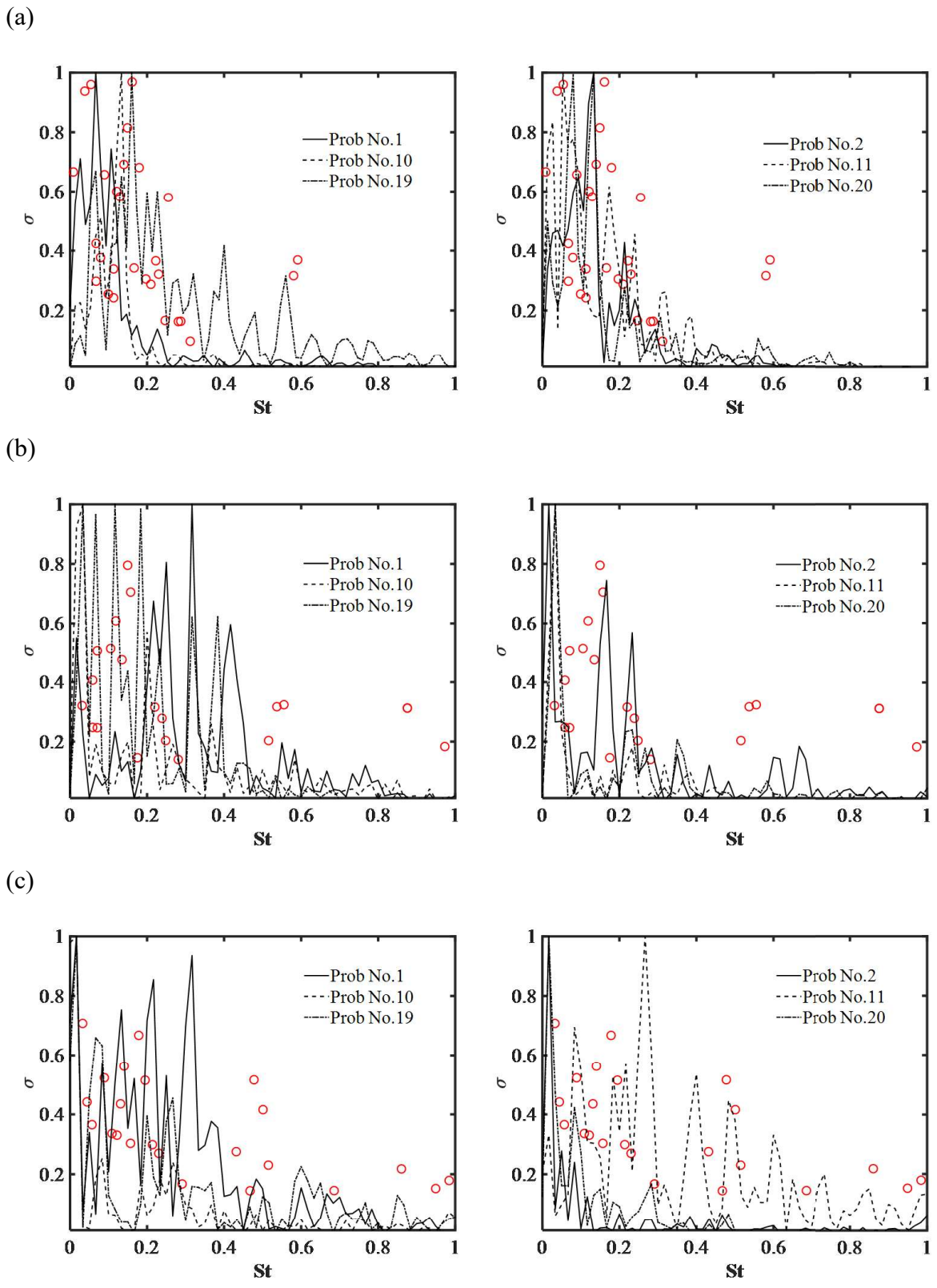

Figure 16. The DMD spectrum (red circles) of the (a) 0° pitch angle case, (b) 15° pitch angle case, (a) -15° pitch angle case obtained by the SPDMD algorithm with $\gamma = 205$ and the PSDs of the streamwise velocity signals at different probes.

Comparing the result of the SPDMD analysis with different γ values, three modes apart from the time-averaged mode are selected to represent the unsteady dominant flow features for each pitch angle. Their spatial characteristic flow structures are revealed in Figures 17-19. Figure 17 shows the DMD modes of the 0° case and three dominant DMD modes are selected for analysis. Figure 17 (b) depicts the streamwise velocity of the DMD mode at $St = 0.113$, which exhibits a double helical spatial structure. As shown in the XZ and XY planes in Figures 17 (b), a pair of large-scale vortex structures are regularly shed from the AUH top and bottom (the XZ plane in Figure 17 (b)) as well as the two-lateral edge (the XY plane in Figure 17 (b)) at the same frequency. According to Ohmichi et al. (2019), these helical structures are related to the rotation of a fluctuation phase in the circumferential direction. Figure 17 (c) shows the mode of $St = 0.068$, whose structure is similar to that of the mode at $St = 0.113$, but the length-scales become larger, which indicated that it is the subharmonic of the mode at $St = 0.113$. Similar helical structures were also reported in Berger et al. (1990), Constantinescu and Squires (2004) and Rodriguez et al. (2011). It was also observed in the wake of a capsule in Ohmichi et al. (2019). As reported in Constantinescu (2004), the helical structures appear behind a sphere at low Reynolds numbers but disappear at a high Reynolds number ($Re = 1.14 \times 10^6$ in their case). However, since the AUH is the shape of an oblate sphere and has many installations resulting in an asymmetrical shape, the topology of the wake structure is dissimilar to that behind a sphere but may be similar to the wake behind a disk. The mode at $St = 0.1054$ for the 15° pitch angle case exhibits a similar helical structure, as shown in Figure 18 (c). However, there is no obvious flow structure at $St \sim 0.1$ for the $-15°$ modes.

Figure 17 (d) shows a low-frequency mode at $St = 0.0086$, and the spatial structure of this mode is significantly different from the other two modes. There is almost no vortex shedding from the right and left edge of the AUH, and only the large-scale flow structures from the top and bottom are observed. Similar to what was reported in Ohmichi et al. (2019), long streamwise vortex structures are present. In the near-wake region, they are located around the recirculation bubbles, especially close to the iUSBL receiver, which may be related to the flapping motion of the wake bubbles as reported in Ohmichi et al. (2019). In the far wake region, the longitude vortical structures correspond to the slow motion of the wake flow in the circumferential direction. As for the other two pitch angle cases, there is a similar flow structure in the dominant modes at $St = 0.0314$ for the 15° pitch angle case shown in Figure 18 (d) as well as the mode at $St = 0.0188$ for the $-15°$ pitch angle case shown in Figure 19 (d). They also exhibit large-scale low-frequency flapping motions only from the top and bottom of the

AUH. However, the frequencies of these modes are higher than that for the 0° case, which indicates the asymmetric pitch angle accelerates the flapping motions. Compared with the 0° case, there is an additional high-frequency mode at $St = 0.8757$ and 0.8604 for the two pitch cases as shown in Figure 18 (b) and Figure 19 (b), respectively, which exhibit small-scale wavy structures along the circumferential direction shedding downstream. These flow structures can be divided into three branches from the two sides and also the top of the AUH. In addition, for these two cases, the high-frequency mode may originate from the propeller tunnel, as shown in the XZ planes in Figure 18 (b) and Figure 19 (b).

(a)

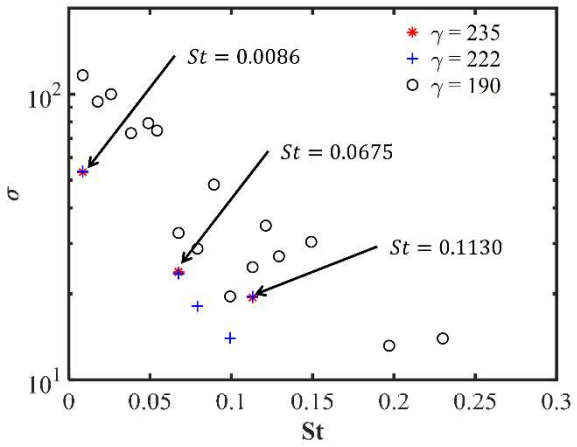

(b)

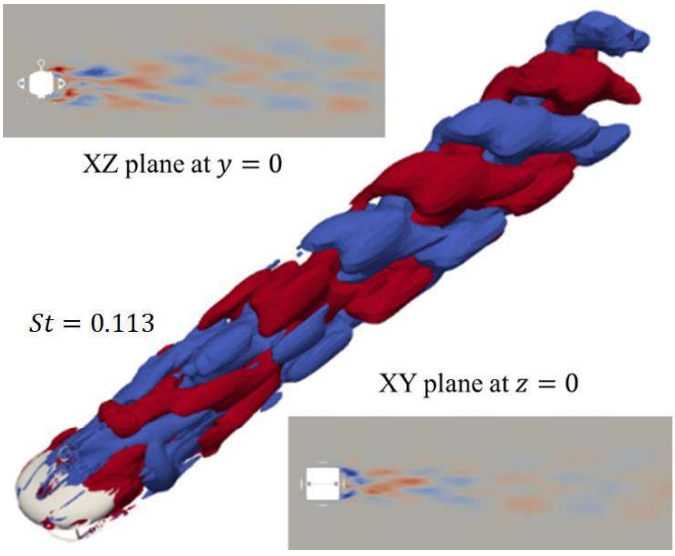

(c)

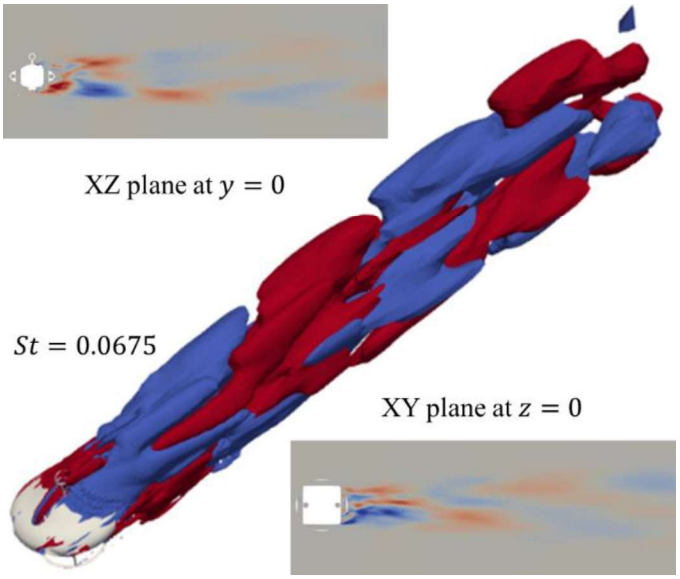

(d)

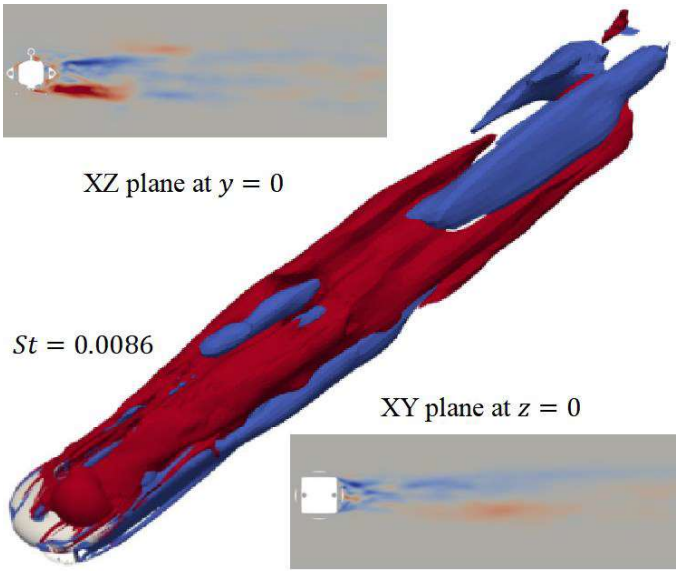

Figure 17. The mode shapes of the 0° pitch angle case. (a) The DMD spectral obtained by the SPDMD algorithm with different γs; (b) The iso-surfaces and the contours on the XZ and XY planes of the streamwise velocity for the $St = 0.113$ mode; (c) The iso-surfaces and the contours on the XZ and XY planes of the streamwise velocity for the $St = 0.0675$ mode; (d) The iso-surfaces and the contours on the XZ and XY planes of the streamwise velocity for the $St = 0.0086$ mode.

(a)

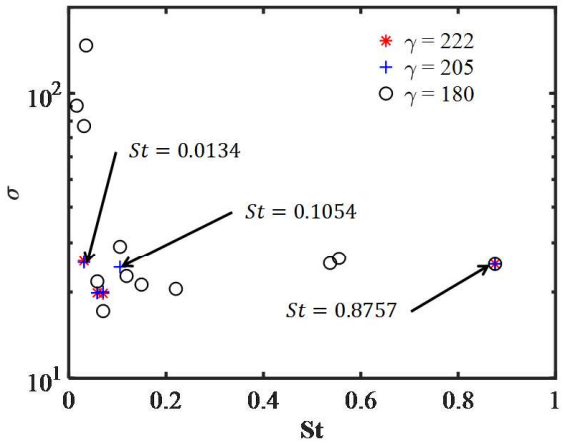
γ = 222
γ = 205
γ = 180
St = 0.0134
St = 0.1054
St = 0.8757
σ
St
10^2
10^1
0
0.2
0.4
0.6
0.8
1

(b)

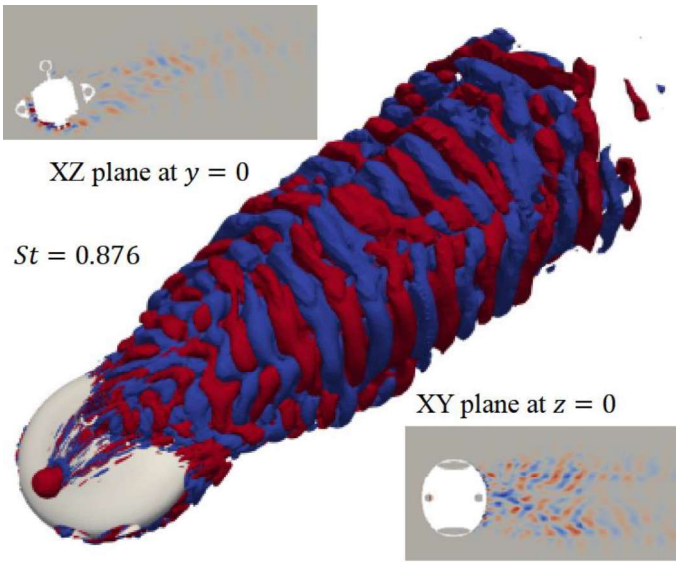
XZ plane at y = 0
St = 0.876
XY plane at z = 0

(c)

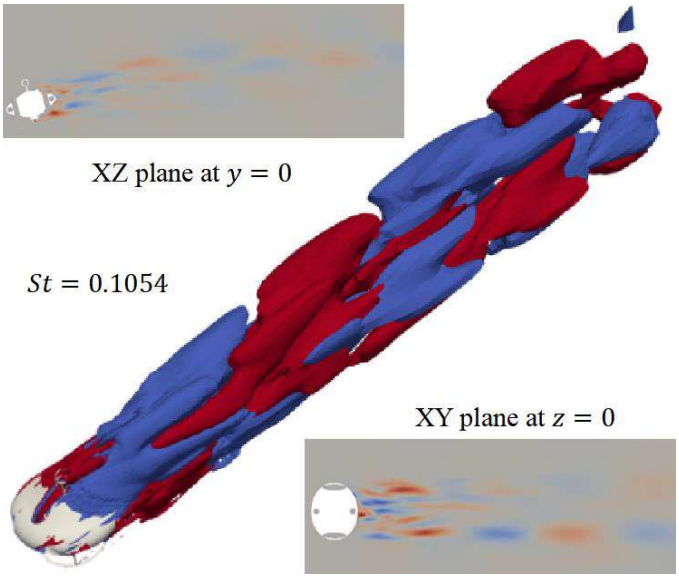

(d)

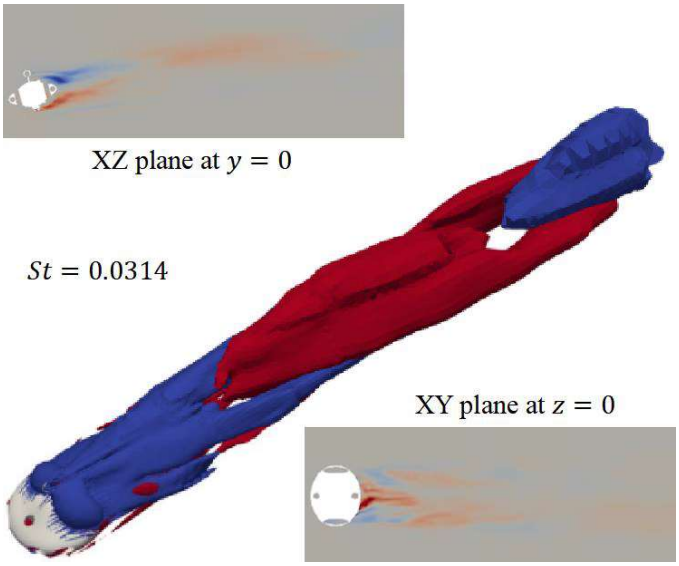

Figure 18. The mode shapes of the 15° pitch angle case. (a) The DMD spectral obtained by the SPDMD algorithm with different γs; (b) The iso-surfaces and the contours on the XZ and XY planes of the streamwise velocity for the $St = 0.876$ mode; (c) The iso-surfaces and the contours on the XZ and XY planes of the streamwise velocity for the $St = 0.105$ mode; (d) The iso-surfaces and the contours on the XZ and XY planes of the streamwise velocity for the $St = 0.0314$ mode.

(a)

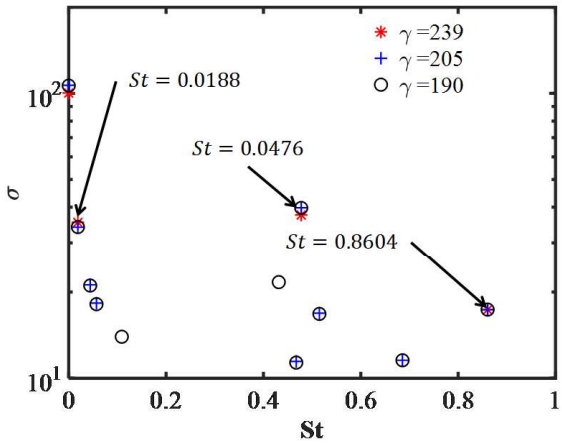
γ=239
γ=205
γ=190
St = 0.0188
St = 0.0476
St = 0.8604
σ
St
10^2
10^1
0
0.2
0.4
0.6
0.8
1

(b)

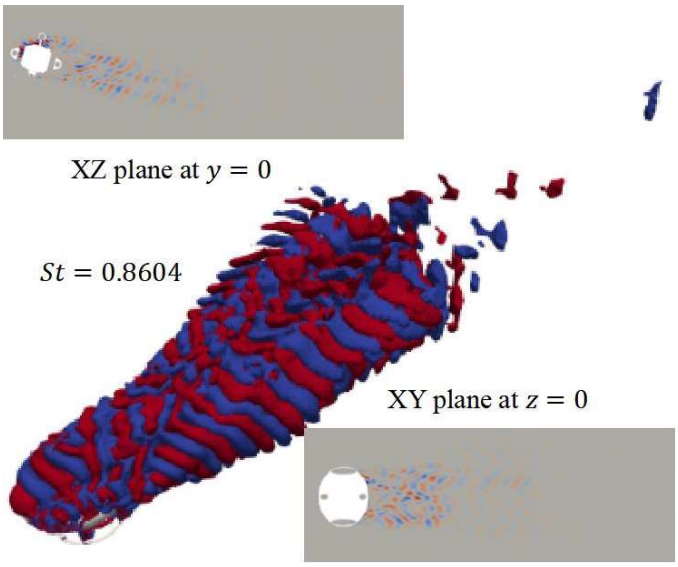
XZ plane at y = 0
St = 0.8604
XY plane at z = 0

(c)

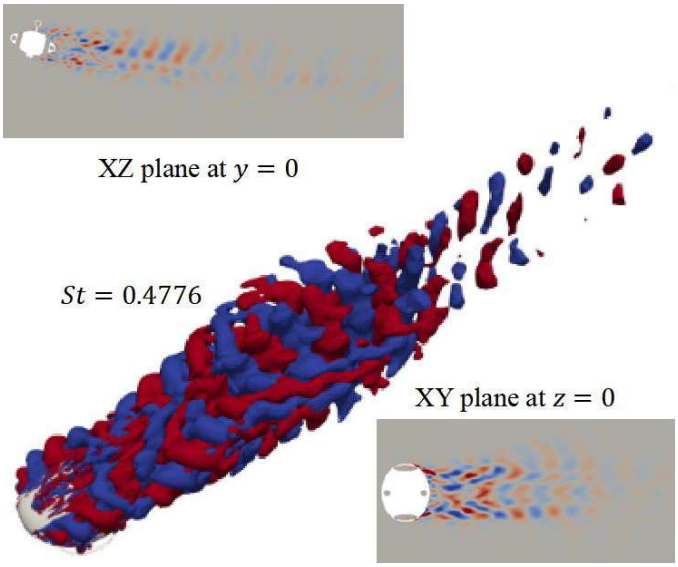

(d)

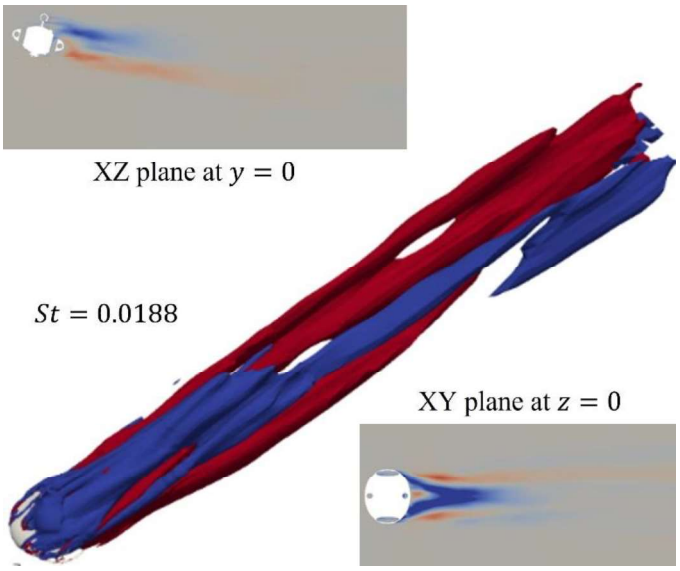

Figure 19. The mode shapes of the $-15°$ pitch angle case. (a) The DMD spectral obtained by the SPDMD algorithm with different γs; (b) The iso-surfaces and the contours on the XZ and XY planes of the streamwise velocity for the $St = 0.8604$ mode; (c) The iso-surfaces and the contours on the XZ and XY planes of the streamwise velocity for the $St = 0.4776$ mode; (d) The iso-surfaces and the contours on the XZ and XY planes of the streamwise velocity for the $St = 0.0188$ mode.

5. Conclusion

A systematic analysis of flow around an AUH is performed using three-dimensional (3D) Improved Delayed Detached Eddy Simulations. Validation studies are carried out by using an oblate sphere with a similar shape to the investigated AUH, and the results demonstrate that the IDDES method is capable of accurately simulating the flow around the AUH. The analysis of the hydrodynamic quantities of the AUH and vortical structures behind the AUH using the drag force element analysis method provides insights into the relationship between the hydrodynamic forces and the surrounding flow structures. Furthermore, Dynamic Mode Decomposition is applied to the flow data in the 3D wake flow, and the dynamic information of the coherent structures in the wake region can be extracted. Overall, the present study provides a detailed understanding of the flow around an AUH and its implications for the design and optimization of underwater vehicles. The main conclusions of this study are outlined as follows:

1. The drag coefficient $\boldsymbol{C_D}$ and the lift coefficient $\boldsymbol{C_L}$ of the AUH increase with the pitch angles. The influence of the asymmetrical structure on these coefficients is reduced with the increasing incoming flow velocity. When the pitch angle increases from 0° to ±15°, the value of the time-averaged $\langle \boldsymbol{C_D} \rangle$ increases from 0.50 to 0.67. For the value of the time-averaged $\langle \boldsymbol{C_L} \rangle$, as the pitch angle increases from -15° to +15°, the value monotonically decreases from 0.73 to -0.89.
2. The vortex structure of the wake flow behind the AUH is significantly different at the positive and negative pitch angles due to the influence of the asymmetric structures installed on the top and bottom of the AUH. The installations on the AUH with different sizes have different contributions to the drag force. The influence of the small-sized GPS antenna can be ignored but the iUSBL sensor-sized structures should be considered when conducting a drag reduction design.
3. DMD analysis is performed for three pitch angle cases subjected to an incoming velocity of 0.5 m/s. By using the sparsity-promoted DMD algorithm, the frequencies and amplitudes of the dominant DMD modes making the most contributions to the inherent dynamics of the flow around the AUH for each pitch angle case are obtained and their corresponding three-dimensional spatial characteristics are revealed. For the $\boldsymbol{0}$° pitch angle case, the dominant DMD mode represents a large-scale vortex shedding phenomenon with a helical organization. The vortex shedding mode is retained in both the $\boldsymbol{15}$° and $\boldsymbol{-15}$° pitch angle cases, but the frequency of these modes becomes higher than that of the $\boldsymbol{0}$° case. The low-

frequency mode is related to the flapping motions of the wake flow and its frequency is also influenced by the installed structures on top and bottom of the AUH.

Acknowledgments

This study was supported with computational resources provided by UNINETT Sigma2—the National Infrastructure for High Performance Computing and Data Storage in Norway under Project No. NN9372K. The first author also acknowledges the support of the China Scholarship Council (CSC).

Author declarations

Conflict of Interest

The authors have no conflicts to disclose.

References

[1]. Stommel, H. (1989). The slocum mission. Oceanography, 2(1), 22-25.

[2]. Hagen, P. E., Storkersen, N. J., & Vestgard, K. (1999, September). HUGIN-use of UUV technology in marine applications. In Oceans' 99. MTS/IEEE. Riding the Crest into the 21st Century. Conference and Exhibition. Conference Proceedings (IEEE Cat. No. 99CH37008) (Vol. 2, pp. 967-972). IEEE.

[3]. Sherman, J., Davis, R. E., Owens, W. B., & Valdes, J. (2001). The autonomous underwater glider" Spray". IEEE Journal of Oceanic Engineering, 26(4), 437-446.

[4]. Bondaryk, J. E. (2004). Bluefin autonomous underwater vehicles: Programs, systems, and acoustic issues. The Journal of the Acoustical Society of America, 115(5), 2615-2615.

[5]. Evans, J., & Nahon, M. (2004). Dynamics modeling and performance evaluation of an autonomous underwater vehicle. Ocean Engineering, 31(14-15), 1835-1858.

[6]. Jagadeesh, P., Murali, K., & Idichandy, V. G. (2009). Experimental investigation of hydrodynamic force coefficients over AUV hull form. Ocean Engineering, 36(1), 113-118.

[7]. Xiang, X., Yu, C., Niu, Z., & Zhang, Q. (2016). Subsea cable tracking by autonomous underwater vehicle with magnetic sensing guidance. Sensors, 16(8), 1335.

[8]. Neves, G., Ruiz, M., Fontinele, J., & Oliveira, L. (2020). Rotated object detection with forward-looking sonar in underwater applications. Expert Systems with Applications, 140, 112870.

[9]. Bettle, M. C., Gerber, A. G., & Watt, G. D. (2009). Unsteady analysis of the six DOF motion of a buoyantly rising submarine. Computers & Fluids, 38(9), 1833-1849.

[10]. Wang, Z., Liu, X., Huang, H., & Chen, Y. (2019). Development of an autonomous underwater helicopter with high maneuverability. Applied Sciences, 9(19), 4072.

[11]. Chen, C. W., Jiang, Y., Huang, H. C., Ji, D. X., Sun, G. Q., Yu, Z., & Chen, Y. (2017). Computational fluid dynamics study of the motion stability of an autonomous underwater helicopter. Ocean Engineering, 143, 227-239.

[12]. Chen, C. W., Wang, T., Feng, Z., Lu, Y., Huang, H., Ji, D., & Chen, Y. (2020). Simulation research on water-entry impact force of an autonomous underwater helicopter. Journal of Marine Science and Technology, 25(4), 1166-1181.

[13]. Lin, Y., Huang, Y., Zhu, H., Huang, H., & Chen, Y. (2021). Simulation study on the hydrodynamic resistance and stability of a disk-shaped autonomous underwater helicopter. Ocean Engineering, 219, 108385.

[14]. Guo, J., Lin, Y., Lin, P., Li, H., Huang, H., & Chen, Y. (2022). Study on hydrodynamic characteristics of the disk-shaped autonomous underwater helicopter over sea-beds. Ocean Engineering, 266, 113132.

[15]. Lin, Y., Guo, J., Li, H., Wang, Z., Chen, Y., & Huang, H. (2022). Improvement of hydrodynamic performance of the disk-shaped autonomous underwater helicopter by local shape modification. Ocean Engineering, 260, 112056.

[16]. Lin, Y., Guo, J., Li, H., Zhu, H., Huang, H., & Chen, Y. (2022). Study on the Motion Stability of the Autonomous Underwater Helicopter. Journal of Marine Science and Engineering, 10(1), 60.

[17]. Schmid, P. J. (2010). Dynamic mode decomposition of numerical and experimental data. Journal of fluid mechanics, 656, 5-28.

[18]. Menter, F. R., Kuntz, M., & Langtry, R. (2003). Ten years of industrial experience with the SST turbulence model. Turbulence, heat and mass transfer, 4(1), 625-632. [M.S. Gritskevich, A.V. Gritskevich, M. S., Garbaruk, A. V., Schütze, J., & Menter, F. R. (2012). Development of DDES and IDDES formulations for the k-ω shear stress transport model. Flow, turbulence and combustion, 88(3), 431-449.

[19]. Uchida, S., Kuwahara, H., Tsuboi, J., Akatsuka, T., Nakata, Y., & Kano, Y. (1981). On the Aerodynamic Properties of the Oblate Spheriod. Aeronautical and Space Sciences Japan, 29(330), 343-349. https://doi.org/10.2322/jjsass1969.29.343.

[20]. Jeong, J., & Hussain, F. (1995). On the identification of a vortex. Journal of fluid mechanics, 285, 69-94.

[21]. Yin, G., & Ong, M. C. (2021). Numerical analysis on flow around a wall-mounted square structure using Dynamic Mode Decomposition. Ocean Engineering, 223, 108647.

[22]. Tian, X., Ong, M. C., Yang, J., & Myrhaug, D. (2014). Large-eddy simulation of the flow normal to a flat plate including corner effects at a high Reynolds number. Journal of Fluids and Structures, 49, 149-169.

[23]. Chang, C. C. (1992). Potential flow and forces for incompressible viscous flow. Proceedings of the Royal Society of London. Series A: Mathematical and Physical Sciences, 437(1901), 517-525.

[24]. Lee, J. J., Hsieh, C. T., Chang, C. C., & Chu, C. C. (2012). Vorticity forces on an impulsively started finite plate. Journal of fluid mechanics, 694, 464-492.

[25]. Zhang, K., Hayostek, S., Amitay, M., He, W., Theofilis, V., & Taira, K. (2020). On the formation of three-dimensional separated flows over wings under tip effects. Journal of Fluid Mechanics, 895, A9.

[26]. Menon, K., & Mittal, R. (2021). On the initiation and sustenance of flow-induced vibration of cylinders: insights from force partitioning. Journal of Fluid Mechanics, 907, A37.

[27]. Ong, M. C., & Yin, G. (2022). On the three-dimensional wake flow behind a normal flat plate. Physics of Fluids, 34(1), 013603.

[28]. Hemmati, A., Wood, D. H., & Martinuzzi, R. J. (2019). Wake dynamics and surface pressure variations on two-dimensional normal flat plates. AIP Advances, 9(4), 045209.

[29]. Schmid, P. J. (2010). Dynamic mode decomposition of numerical and experimental data. Journal of fluid mechanics, 656, 5-28.

[30]. Jovanović, M. R., Schmid, P. J., & Nichols, J. W. (2014). Sparsity-promoting dynamic mode decomposition. Physics of Fluids, 26(2), 024103.

[31]. Ohmichi, Y. (2017). Preconditioned dynamic mode decomposition and mode selection algorithms for large datasets using incremental proper orthogonal decomposition. AIP Advances, 7(7), 075318.

[32]. Ohmichi, Y., Kobayashi, K., & Kanazaki, M. (2019). Numerical investigation of wake structures of an atmospheric entry capsule by modal analysis. Physics of Fluids, 31(7), 074105.

[33]. Schmid, P. J. (2011). Application of the dynamic mode decomposition to experimental data. Experiments in fluids, 50, 1123-1130.

[34]. Pan, C., Xue, D., & Wang, J. (2015). On the accuracy of dynamic mode decomposition in estimating instability of wave packet. Experiments in Fluids, 56, 1-15.

[35]. Welch, P. (1967). The use of fast Fourier transform for the estimation of power spectra: a method based on time averaging over short, modified periodograms. IEEE Transactions on audio and electroacoustics, 15(2), 70-73.

[36]. Taira, K., Brunton, S. L., Dawson, S. T., Rowley, C. W., Colonius, T., McKeon, B. J., ... & Ukeiley, L. S. (2017). Modal analysis of fluid flows: An overview. Aiaa Journal, 55(12), 4013-4041.

[37]. Berger, E., Scholz, D., & Schumm, M. (1990). Coherent vortex structures in the wake of a sphere and a circular disk at rest and under forced vibrations. Journal of Fluids and Structures, 4(3), 231-257.

[38]. Constantinescu, G., & Squires, K. (2004). Numerical investigations of flow over a sphere in the subcritical and supercritical regimes. Physics of Fluids, 16(5), 1449-1466.

[39]. Rodriguez, I., Borell, R., Lehmkuhl, O., Segarra, C. D. P., & Oliva, A. (2011). Direct numerical simulation of the flow over a sphere at Re= 3700. Journal of Fluid Mechanics, 679, 263-287.